
Ammonia mapping observations of the Galactic infrared bubble N49: Three NH₃ clumps along the molecular filament

Mikito KOHNO^{1,2*}, James O. CHIBUEZE^{3,4}, Ross A. BURNS⁵, Toshihiro OMODAKA⁶, Toshihiro HANNA^{6,7}, Takeru MURASE⁶, Rin I. YAMADA², Takumi NAGAYAMA⁸, Makoto NAKANO⁹, Kazuyoshi SUNADA⁸, Kengo TACHIHARA² and Yasuo FUKUI²

¹Astronomy Section, Nagoya City Science Museum, 2-17-1 Sakae, Naka-ku, Nagoya, Aichi 460-0008, Japan

²Department of Physics, Graduate School of Science, Nagoya University, Furo-cho, Chikusa-ku, Nagoya, Aichi 464-8602, Japan

³Centre for Space Research, Potchefstroom campus, North-West University, Potchefstroom 2531, South Africa

⁴Department of Physics and Astronomy, Faculty of Physical Sciences, University of Nigeria, Carver Building, 1 University Road, Nsukka 410001, Nigeria

⁵National Astronomical Observatory of Japan (NAOJ), National Institutes of Natural Sciences (NINS), 2-21-1 Osawa, Mitaka, Tokyo 181-8588, Japan

⁶Graduate School of Science and Engineering, Kagoshima University, 1-21-35 Korimoto, Kagoshima, Kagoshima 890-0065, Japan

⁷Amanogawa Galaxy Astronomy Research Center (AGARC), Kagoshima University, 1-21-35 Korimoto, Kagoshima, Kagoshima 890-0065, Japan

⁸Mizusawa VLBI Observatory, National Astronomical Observatory of Japan, Osawa 2-21-1, Mitaka-shi, Tokyo 181-8588, Japan

⁹Faculty of Science and Technology, Oita University, 700 Dannoharu, Oita, Oita 870-1192,

Japan

*E-mail: mikito.kohno@gmail.com, kohno@nagoya-p.jp

Received 2022 October 11; Accepted 2023 January 19

Abstract

We have carried out the NH_3 (J, K) = (1,1), (2,2), and (3,3) mapping observations toward the Galactic infrared bubble N49 (G28.83–0.25) using the Nobeyama 45 m telescope. Three NH_3 clumps (A, B, and C) were discovered along the molecular filament with the radial velocities of ~ 96 , 87, and 89 km s^{-1} , respectively. The kinetic temperature derived from the NH_3 (2,2)/ NH_3 (1,1) shows $T_{\text{kin}} = 27.0 \pm 0.6$ K enhanced at Clump B in the eastern edge of the bubble, where position coincides with massive young stellar objects (MYSOs) associated with the 6.7 GHz class II methanol maser source. This result shows the dense clump is locally heated by stellar feedback from the embedded MYSOs. The NH_3 Clump B also exists at the 88 km s^{-1} and 95 km s^{-1} molecular filament intersection. We therefore suggest that the NH_3 dense gas formation in Clump B can be explained by a filament-filament interaction scenario. On the other hand, NH_3 Clump A and C at the northern and southern side of the molecular filament might be the sites of spontaneous star formation because these clumps are located ~ 5 –10 pc away from the edge of the bubble.

Key words: ISM: H II regions — ISM: clouds — ISM: molecules — ISM: bubbles — stars: formation — ISM: individual objects (N49, G028.83-0.25)

1 Introduction

Ionized hydrogen (H II) regions are formed by the ultra-violet radiation from OB-type stars. They are known to be sites of triggered star formation from previous works of observations and theories (e.g., Elmegreen 1998) and are also identified as “interstellar bubbles” (e.g., Castor et al. 1975; Weaver et al. 1977). For example, the Galactic Legacy Infrared Mid-Plane Survey Extraordinaire (GLIMPSE) by the Spitzer space telescope found ~ 600 infrared bubbles in the Galactic plane ($|l| \leq 65^\circ$, $|b| \leq 1^\circ$: Churchwell et al. 2006; Churchwell et al. 2007). Most of them are H II regions excited by OB-type stars inside the bubbles (Deharveng et al. 2010). Two star formation scenarios regarding bubbles have recently been discussed as “collect-and-collapse” (Deharveng et al. 2010) and “cloud-cloud collisions” (Fukui et al. 2021) based on their morphology and distributions of parent clouds. The

former is shock compression by the expansion of H II regions which triggers second generation star formation at the edge of the bubble (e.g., Elmegreen & Lada 1977; Whitworth et al. 1994; Deharveng et al. 2005; Hosokawa & Inutsuka 2006; Zavagno et al. 2006; Zavagno et al. 2007; Dale et al. 2007; Thompson et al. 2012; Xu & Ju 2014; Palmeirim et al. 2017; Li et al. 2019; Luisi et al. 2021). The latter is the two clouds with different sizes colliding, triggering the formation of exciting stars and forming arc-like morphology (e.g., Habe & Ohta 1992; Hasegawa et al. 1994; Higuchi et al. 2014; Torii et al. 2015; Baug et al. 2016; Fukui et al. 2018; Ohama et al. 2018; Koide et al. 2019; Fujita et al. 2019; Kohno et al. 2021b; Yamada et al. 2021; Enokiya & Fukui 2022). These scenarios are possibly related to infrared bubbles, however, the dominant mechanism remains unclear.

N49 (also known as G28.83–0.25) is an infrared bubble at $(l, b) \sim (28^\circ 83, -0^\circ 23)$ in the Galactic plane (Zavagno et al. 2010), which is identified as a “closed bubble” based on AKARI 9 μm infrared morphology (Hattori et al. 2016; Hanaoka et al. 2019; Hanaoka et al. 2020). It has been studied as a representative “wind-blown bubble” (Everett & Churchwell 2010). The distance to N49 from the solar system is 5.07 kpc associated with the Scutum Arm (Dirienzo et al. 2012; Dewangan et al. 2017). Figure 1(a) shows the three-color composite image of the Spitzer space telescope (Werner et al. 2004). Blue, green, and red present the 3.6 μm , 8.0 μm , and 24 μm images, respectively. These bands trace the thermal emission from the stars, polycyclic aromatic hydrocarbons (PAH) emission in the photo-dissociation region (e.g., Draine & Li 2007; Draine 2003), and hot dust heated by OB-type stars (e.g., Carey et al. 2009), respectively. Figure 1(b) presents the close-up image of the N49 bubble. White contours indicate the Very Large Array (VLA) 1.4 GHz continuum image, which traces distributions of the ionized gas. The distribution of the ionized gas coincide the hot dust emission traced by Spitzer 24 μm image. YSO #1, YSO #3, and the ultra-compact H II region (UCH II) exist at the bubble’s eastern edge (see Figure 18 in Deharveng et al. 2010). Previous studies reported that YSO #3 is associated with the 6.7 GHz class II methanol maser embedded in the massive YSOs and referred to as extended green objects (EGOs: Cyganowski et al. 2008; Cyganowski et al. 2009, and see also data base of astrophysical masers Ladeyschikov et al. 2019¹). Figure 1(c) shows the ^{13}CO $J=1-0$ peak intensity map obtained by the Nobeyama 45 m telescope (Umemoto et al. 2017; Torii et al. 2019). The optically thinner ^{13}CO $J=1-0$ can trace a molecular hydrogen density of $n(\text{H}_2) \sim 10^3 \text{ cm}^{-3}$ (e.g., Solomon et al. 1979; Nagahama et al. 1998; Kawamura et al. 1998; Jackson et al. 2006; Torii et al. 2019). Thus, it is appropriate to study the large-scale structure in the surrounding of the dense gas. ^{13}CO has the filamentary structure and arc-like morphology around the ionized gas at the eastern side of the N49 bubble (see also Figure 12 in Yan et al. 2016).

Previous studies of the N49 bubble suggested triggering of star formation by expanding H II

¹ <https://maserdb.net/object.pl?object=G28.833-0.252>

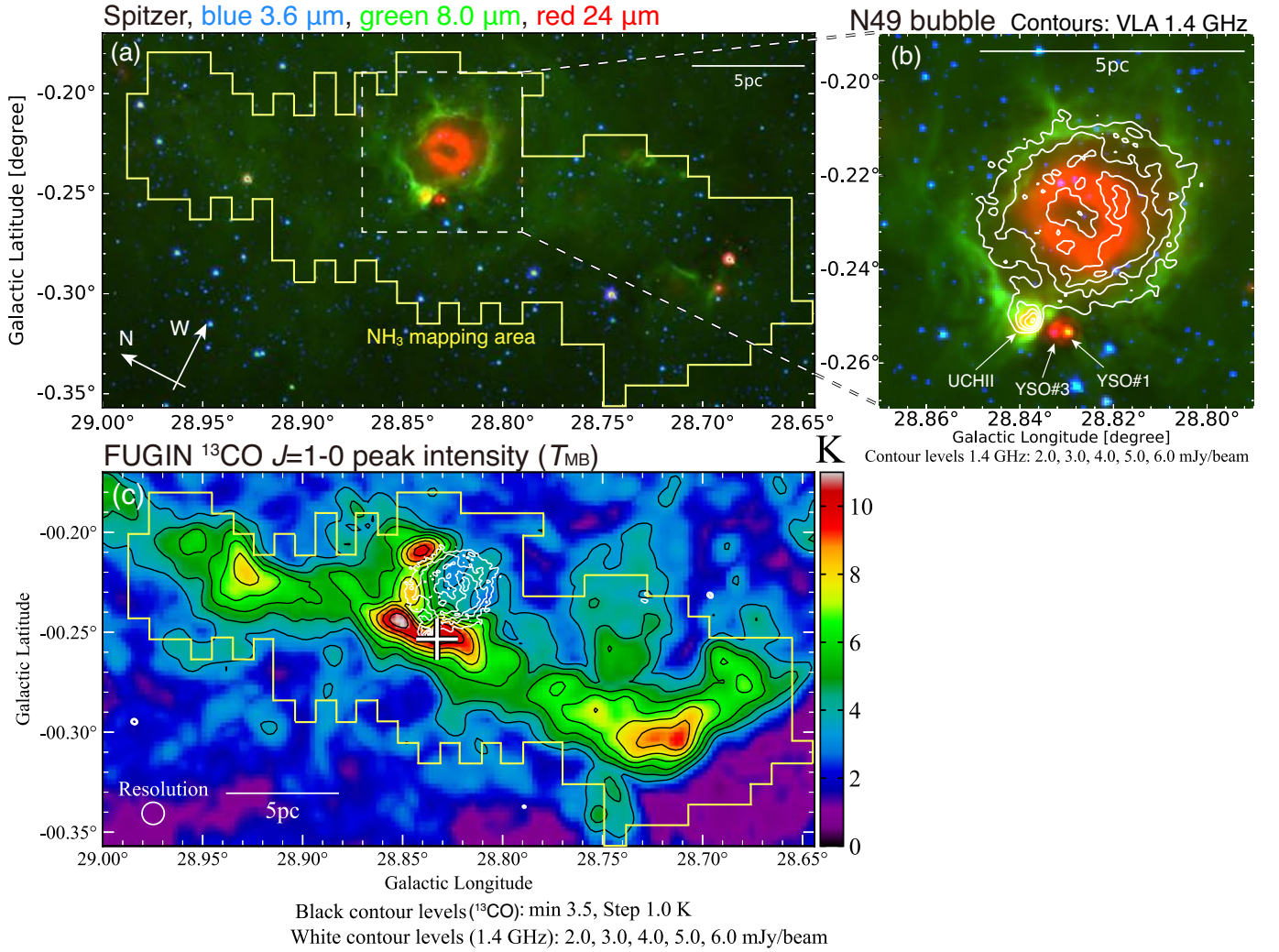


Fig. 1. (a) Spitzer three color composite image of the infrared bubble N49. Blue, green, and red show $3.6 \mu\text{m}$, $8.0 \mu\text{m}$, and $24 \mu\text{m}$, respectively. Yellow enclosed area indicates the NH_3 mapping region of our project. (b) The close-up image of (a). White contours show the VLA 1.4 GHz continuum image (Helfand et al. 2006). The lowest contour level and interval are 2 and 1 mJy/beam, respectively. The ultra-compact H II region, YSO #1, and YSO #3 are labeled (see Figure 18 in Deharveng et al. 2010 and Watson et al. 2008). (c) The peak intensity (T_{MB}) map of ^{13}CO $J = 1-0$ obtained by the FUGIN project (Umemoto et al. 2017; Torii et al. 2019). The black lowest contour level and interval are 3.5 and 1.0 K, respectively. White contours show the VLA 1.4 GHz continuum image. The white contour levels are 2.0, 3.0, 4.0, 5.0, and 6.0 mJy/beam. The white cross indicates the position of the 6.7 GHz class II methanol maser source (Cyanowski et al. 2008; Cyanowski et al. 2009).

region (Watson et al. 2008; Dirienzo et al. 2012). Xu et al. (2019) performed CO observations toward the molecular filament and bubble. The authors argue that feedback from the H II region affects star formation and helps to drive the turbulence in the filament. On the other hand, Dewangan et al. (2017) found two different radial velocity filaments associated with the bubble. They argued that the filament-filament collision scenario could explain the massive star formation at the edge of the bubble.

Star formation scenarios are discussed in previous works, while the dense gas formation mech-

anism related to star formation of the N49 bubble and the molecular filament is not yet clear. The NH₃ emission can trace dense gas ($n(\text{H}_2) \gtrsim 10^4 \text{ cm}^{-3}$) and derive the kinetic temperature of molecular gas because of the excitation of the NH₃ inversion transitions in the lowest metastable rotational energy states at low temperatures. It also allows us to derive the optical depth and column density, using the splitting of the inversion transitions into different hyperfine structure components around 23GHz (e.g., Cheung et al. 1968; Cheung et al. 1969; Morris et al. 1973; Walmsley & Ungerechts 1983; Ho & Townes 1983). Previous studies of NH₃ observations toward the N49 bubble focused only on the dust clumps identified by the APEX Telescope Large Area Survey of the Galaxy (ATLASGAL: e.g., Wienen et al. 2012). In order to trace the large-scale structure of the environment around the dust clumps, we performed mapping observations (of about 30 pc) of the NH₃ inversion transition of $(J, K) = (1, 1), (2, 2)$, and $(3, 3)$ using the Nobeyama 45 m telescope (see the yellow enclosed area in Figure 1a and c). J and K are the quantum number of the total angular momentum and their projection along the molecular axis (Ho & Townes 1983). In this paper, we adopted the energy levels of each NH₃ transition from the Jet Propulsion Laboratory (JPL) spectral line catalog² (Pickett et al. 1998). This paper is structured as follows: section 2 introduces observations and the archive data; section 3 presents the NH₃ results; in section 4, we discuss dense gas and star formation scenarios in three NH₃ clumps along the molecular filament, and in section 5, we show a summary of this paper.

2 Observations

Table 1. Properties of our observations.

Telescope	Molecule	Transition	E_u/k_{B}	ν_0	Receiver	Grid	HPBW	Velocity	RMS noise
(1)	(2)	(3)	(4)	(5)	(6)	(7)	(8)	(9)	(10)
Nobeyama 45 m	NH ₃	$(J, K) = (1, 1)$	23.3	23.694	H22	37''5	75''	0.39 km s ⁻¹	$\sim 0.03 \text{ K}$
	NH ₃	$(J, K) = (2, 2)$	64.4	23.723	H22	37''5	75''	0.39 km s ⁻¹	$\sim 0.03 \text{ K}$
	NH ₃	$(J, K) = (3, 3)$	123.5	23.870	H22	37''5	75''	0.39 km s ⁻¹	$\sim 0.03 \text{ K}$

Columns: (1) Telescope name (2) Molecules (3) Transitions. J and K are the quantum number of total angular momentum and their projection along the molecular axis, respectively. (4) Upper energy levels (E_u) of inversion transitions above the ground state divided by the Boltzmann constant (k_{B}). (5) Rest frequency (ν_0) (6) Receiver name (7) Grid spacing of the multi-ON- OFF switching observations (8) Half-power beam width (9) Velocity resolution (10) r.m.s noise level of the T_{MB} scale.

2.1 The KAGONMA project: NH₃ mapping observations using the Nobeyama 45 m telescope

We carried out the NH₃ $(J, K) = (1, 1), (2, 2)$, and $(3, 3)$ mapping observations using the Nobeyama

² <https://spec.jpl.nasa.gov>

45 m telescope led by Kagoshima University. Our NH_3 survey project is also called “KAGONMA”³ (Kagoshima galactic object survey with the Nobeyama 45-metre telescope by mapping in ammonia lines) and making use of this survey papers on the Galactic Center and massive star forming regions were published (Nagayama et al. 2007; Nagayama et al. 2009; Toujima et al. 2011; Chibueze et al. 2013; Nakano et al. 2017; Burns et al. 2019; Murase et al. 2022; Kohno et al. 2022; Hirata et al. 2022). We utilized the dual-polarization and the multi-ON-OFF switching (three ON points per one OFF point) mode. The observational period was from December 2014 to June 2015 (PI T. Omodaka: BU145001⁴). The half-power beam width (HPBW) and grid spacing was $75''$ at 23 GHz and $37''.5$, respectively. We used the High Electron Mobility Transistor (HEMT) receiver named H22 at 22 GHz as the front-end. The pointing accuracy was checked within $5''$ observing the H_2O maser source OH43.8-0.1 ($\alpha_{\text{J}2000}, \delta_{\text{J}2000}$) = ($19^{\text{h}}11^{\text{m}}54^{\text{s}}$, $+09^{\text{d}}35'55''$) before starting observations. The FX-type digital spectrometer was used as the back-end system. It is named Spectral Analysis Machine of the 45 m telescope (SAM 45 :Kuno et al. 2011; Kamazaki et al. 2012). The system noise temperature (T_{sys}) including the atmosphere was 150-250 K during observations. We used 8 intermediate frequencies (IFs) to observe the NH_3 (J, K) = (1, 1), (2, 2), (3, 3), and H_2O maser with the dual-polarization simultaneously. Each IF’s frequency bandwidth and resolution were 125 MHz and 30.52 kHz corresponding to the velocity coverage of 1600 km s^{-1} and spacing of 0.39 km s^{-1} at 23 GHz, respectively. The chopper wheel method was adopted to calibrate to the intensity of the antenna temperature (T_a^* : Ulich, & Haas 1976; Kutner, & Ulich 1981). We used the NEWSTAR software package (Ikeda et al. 2001)⁵ to make the cube file from the raw data. We subtract baselines with a first-order polynomial function from the spectra. The baseline ranges were set up emission-free channels of each spectrum. Then, we applied the hanning smoothing (width=5) in the velocity domain to improve the signal-to-noise ratio. The antenna temperature was converted to the main-beam temperature (T_{MB}) using the relation of $T_{\text{MB}} = T_a^*/\eta_{\text{MB}}$. The main-beam efficiency (η_{MB}) is 0.835, the average value of two channels of the H22 receiver in the Nobeyama 45 m telescope. The kinetic temperature and physical parameters are not dependent on the main-beam efficiency because we can derive them from intensity ratios of different transitions around 23 GHz obtained by the same instrument of a radio telescope. The root-mean-square noise level for the final data was $\sim 0.03 \text{ K}$ at the T_{MB} scale (corresponding to $\sim 0.025 \text{ K}$ at the T_a^* scale). The parameters of our NH_3 data are summarized in Table 1.

³ See also conference proceedings by Handa et al. (2006); Murase et al. (2020); Takeba et al. (2022).

⁴ <https://www.nro.nao.ac.jp/~nro45mrt/html/prop/accept/accept2014.html>

⁵ <https://www.nro.nao.ac.jp/~nro45mrt/html/obs/newstar/index.html>

2.2 Archival data

We utilized the ^{13}CO $J = 1\text{-}0$ data comparing with NH_3 spatial and velocity distributions. It was obtained by the FOREST Unbiased Galactic plane Imaging survey with the Nobeyama 45-m telescope (FUGIN⁶: Umemoto et al. 2017; Kohno et al. 2018; Nishimura et al. 2018, 2021; Torii et al. 2019; Sofue et al. 2019; Nakanishi et al. 2020; Sato et al. 2021; Fujita et al. 2021; Kohno et al. 2021a). The FUGIN CO survey adopted the On-the-fly (OTF) mapping mode (Sawada et al. 2008) and used the FOOr-beam REceiver System on the 45m Telescope (FOREST) with the four beams, dual-polarization, side-band separating receiver (Minamidani et al. 2016; Nakajima et al. 2019). The HPBW and effective resolution convolved by the Gaussian kernel function is $15''$ and $21''$ at 110 GHz, respectively. The effective velocity resolution is 1.3 km s^{-1} . Smoothing the data cube by a Gaussian kernel function resulted in a resolution of $\sim 40''$. The r.m.s noise level is $\sim 0.3 \text{ K}$ at the main beam temperature scale. We used the 1.4 GHz ($= 20 \text{ cm}$) radio continuum image with the angular resolution of $\sim 6''$ taken from the Multi-Array Galactic Plane Imaging Survey (MAGPIS) with VLA (White et al. 2005; Helfand et al. 2006). The 1.4 GHz radio continuum image is useful to investigate the free-free emission corresponding to the ionized gas from H II regions. We also obtained the archive data of the Spitzer Space telescope with the wavelength of $3.6 \mu\text{m}$, $8 \mu\text{m}$ (Benjamin et al. 2003; Churchwell et al. 2009), and $24 \mu\text{m}$ (Carey et al. 2009). The $870 \mu\text{m}$ dust continuum image is also taken from ATLASGAL⁷ (Schuller et al. 2009). These fits cubes were taken from the MAGPIS web page⁸.

2.3 Software packages

In this paper, we used the following software packages to create the maps, extract the spectra, and calculate physical parameters (Astropy: Astropy Collaboration et al. 2013; Astropy Collaboration et al. 2018, NumPy: van der Walt et al. 2011, Matplotlib: Hunter 2007, IPython: Perez, & Granger 2007, Miriad: Sault et al. 1995, and APLpy: Robitaille & Bressert 2012).

3 Results

3.1 NH_3 spatial distributions

Figure 2 shows the peak temperature map of the main line in (a) NH_3 ($J, K = (1, 1)$), (b) NH_3 ($2, 2$), and (c) NH_3 ($3, 3$). The white contours present the ionized gas distribution traced by the VLA 1.4 GHz radio continuum image. We identified three clumps in the NH_3 ($1, 1$) line as revealed by the

⁶ <https://nro-fugin.github.io>

⁷ <http://www3.mpifr-bonn.mpg.de/div/atlasgal/>

⁸ <https://third.ucllnl.org/gps/>

intensity peaks along the molecular filament (Figure 2a). Hereafter, we called these clumps “Clump A”, “Clump B”, and “Clump C”. The NH_3 (1,1) peak in Clump B exists on the eastern side of the N49 bubble offset from the ionized gas. We detected the NH_3 (2,2) in Clump A, B, and C (Figure 2b). The NH_3 (3,3) emission is enhanced in Clump B at the eastern edge of the bubble (Figure 2c).

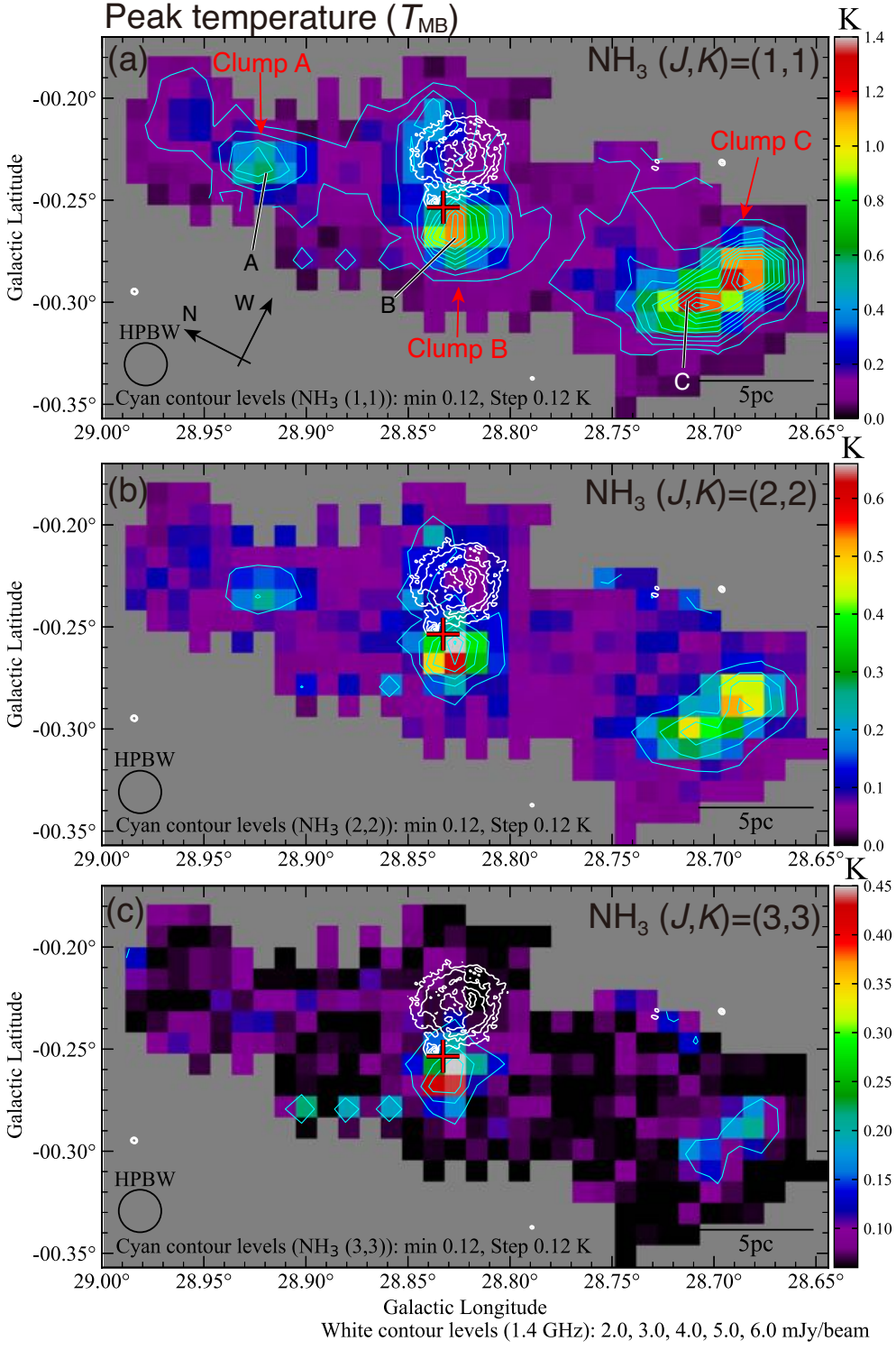


Fig. 2. Peak intensity (T_{MB}) map of (a) $\text{NH}_3 (J, K) = (1, 1)$, (b) $\text{NH}_3 (2, 2)$, and (c) $\text{NH}_3 (3, 3)$. The lowest cyan contour level and intervals of NH_3 are 0.12 K ($\sim 4\sigma$) and 0.12 K ($\sim 4\sigma$), respectively. Three NH_3 clumps are labeled in panel (a). A, B, and C show the positions of the spectra in Figure 3. The white contour levels of the VLA 1.4 GHz continuum image are 2.0, 3.0, 4.0, 5.0, and 6.0 mJy/beam. Red cross indicates the position of the 6.7 GHz class II methanol maser source (Cyanowski et al. 2008; Cyanowski et al. 2009).

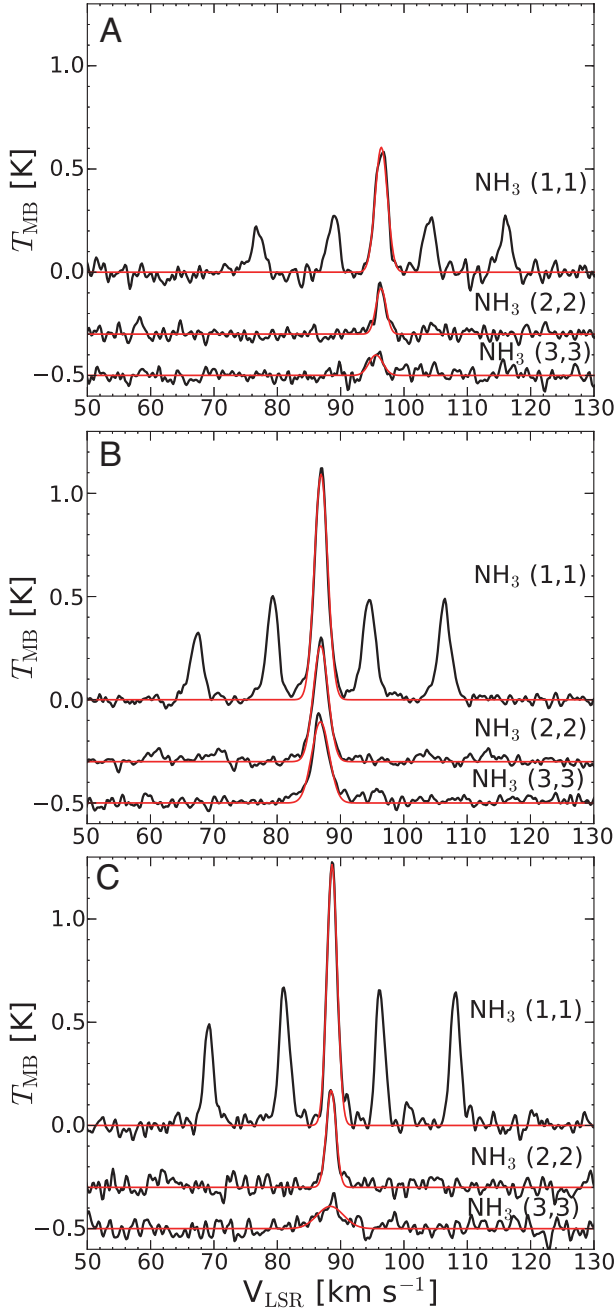


Fig. 3. NH_3 spectra at A ($l, b = (28^\circ.921, -0^\circ.237)$), B ($l, b = (28^\circ.827, -0^\circ.268)$), and C ($l, b = (28^\circ.712, -0^\circ.299)$). These positions are also presented in Figure 2(a). Red lines show the results from a Gaussian function fitted to the emission at the main component. NH_3 (1,1) emissions include four satellite components of $F_1 = 1 \rightarrow 0$, $F_1 = 1 \rightarrow 2$, $F_1 = 2 \rightarrow 1$, and $F_1 = 0 \rightarrow 1$ (from left to right on the velocity axis).

Figure 3 shows the NH_3 peak spectrum at Clump A, B, and C. The locations of each spectrum are labeled in Figure 2(a). In the NH_3 (1,1) emission, the main line exists as the center velocity of each spectrum. We also detected the hyper-fine structures of the inner ($F_1 = 1 \rightarrow 2, 2 \rightarrow 1$) and outer satellite lines ($F_1 = 1 \rightarrow 0, 0 \rightarrow 1$), where F_1 is the quantum number of the angular momentum, contributing to the nitrogen nuclear-spin. The intensity peak of NH_3 (1,1) exists at Clump C, while

NH_3 (3,3) has a peak intensity at Clump B. We derived the peak temperature, peak velocity, and full-width half maximum (FWHM: hereafter, we call it the line width) obtained by a Gaussian fitting toward the main line of each profile. The profile parameters are summarized in Table 2. The errors are the standard deviations of each fitting parameter.

Table 2. NH_3 spectra parameters of the main line in each NH_3 clump

Name	l	b	Transition	T_{MB}	v_{LSR}	Δv
	[degree]	[degree]	(J, K)	[K]	[km s $^{-1}$]	[km s $^{-1}$]
(1)	(2)	(3)	(4)	(5)	(6)	(7)
A	28.921	−0.237	(1,1)	0.61 ± 0.02	96.4 ± 0.04	2.3 ± 0.10
			(2,2)	0.22 ± 0.01	96.4 ± 0.05	1.9 ± 0.11
			(3,3)	0.10 ± 0.01	95.6 ± 0.12	2.6 ± 0.29
B	28.827	−0.268	(1,1)	1.09 ± 0.04	86.9 ± 0.02	2.5 ± 0.10
			(2,2)	0.56 ± 0.007	86.9 ± 0.02	2.8 ± 0.04
			(3,3)	0.39 ± 0.007	86.8 ± 0.03	3.3 ± 0.06
C	28.712	−0.299	(1,1)	1.26 ± 0.05	88.7 ± 0.04	1.9 ± 0.10
			(2,2)	0.47 ± 0.01	88.5 ± 0.03	1.8 ± 0.06
			(3,3)	0.11 ± 0.008	88.4 ± 0.19	4.9 ± 0.44

Columns: (1) Name of each spectra (2) Galactic Longitude (3) Galactic Latitude (4) Rotational transition (5) Peak temperature (T_{MB}) (6) Peak velocity by a single Gaussian fitting (7) The line width ($2\sigma\sqrt{2\ln 2}$) of spectra by a Gaussian fitting, where σ is the standard deviation of the line profile. The errors are the standard deviations of each fitting parameter.

3.2 Three NH_3 clumps with the different radial velocity

Figure 4, 5, and 6 show the NH_3 (1,1), NH_3 (2,2), and NH_3 (3,3) velocity channel map, respectively. Clump A, B, and C has an intensity peak of all transitions at $96\text{--}97 \text{ km s}^{-1}$ (panel i in Figure 4-6), $85\text{--}88 \text{ km s}^{-1}$ (panel b and c in Figure 4-6), and $88\text{--}90 \text{ km s}^{-1}$ (panel d in Figure 4-6), respectively. Clump A and B connect with the diffuse NH_3 (1,1) emission of $94\text{--}97 \text{ km s}^{-1}$ (Figure 4h and 4i). To investigate the velocity field of each clump in more detail, we made the peak velocity and line width map of the NH_3 (1,1) main line obtained by a Gaussian fitting toward a profile at each pixel.

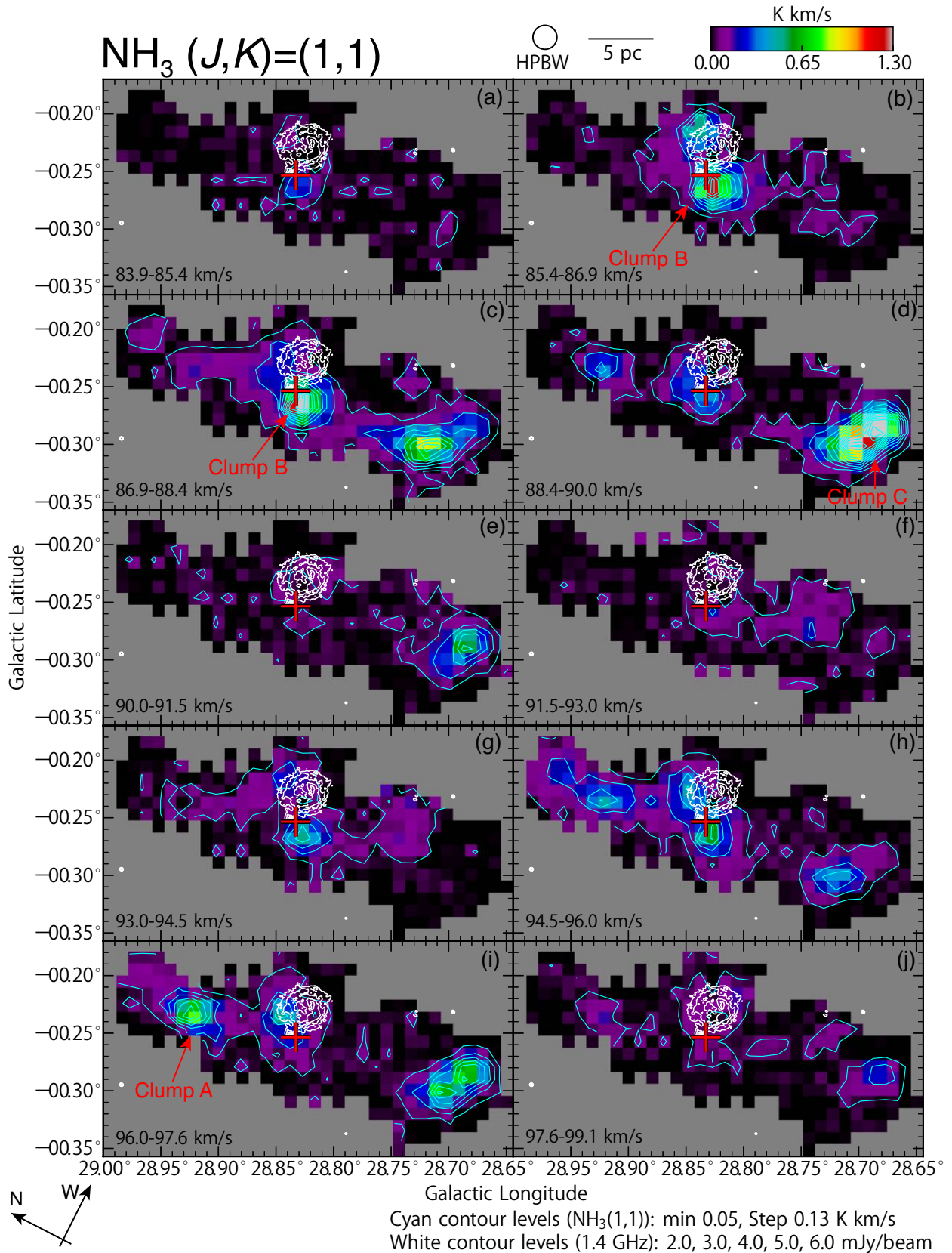


Fig. 4. Velocity channel map of $\text{NH}_3 (J, K) = (1, 1)$. The lowest cyan contour level and intervals are 0.05 K km s^{-1} ($\sim 3\sigma$) and 0.13 K km s^{-1} ($\sim 8\sigma$), respectively. The red cross and white contours are the same as in Figure 2a. The white contour levels of the VLA 1.4 GHz continuum image are 2.0, 3.0, 4.0, 5.0, and 6.0 mJy/beam.

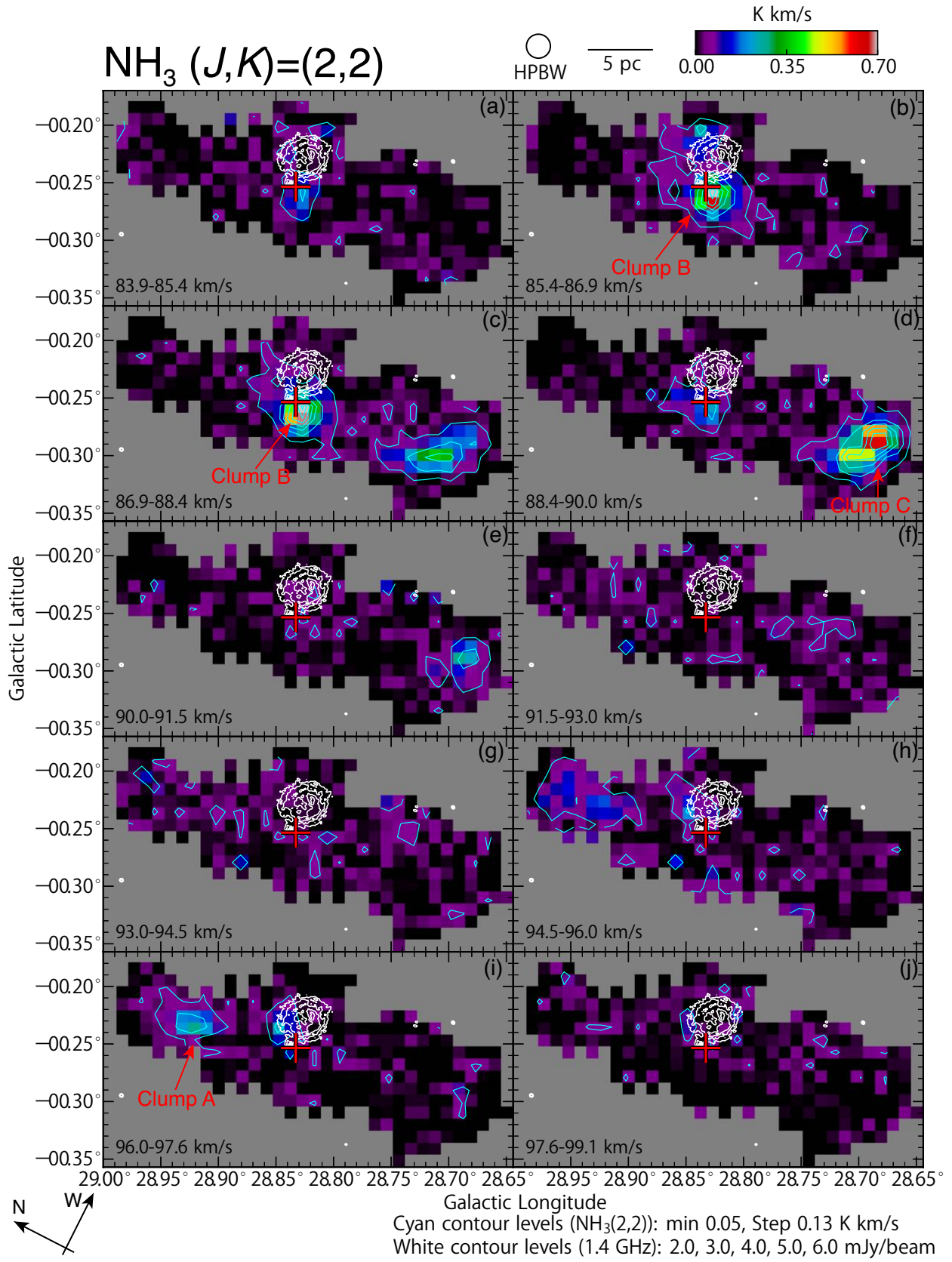


Fig. 5. Same as Figure 4, but for $\text{NH}_3 (J,K) = (2,2)$.

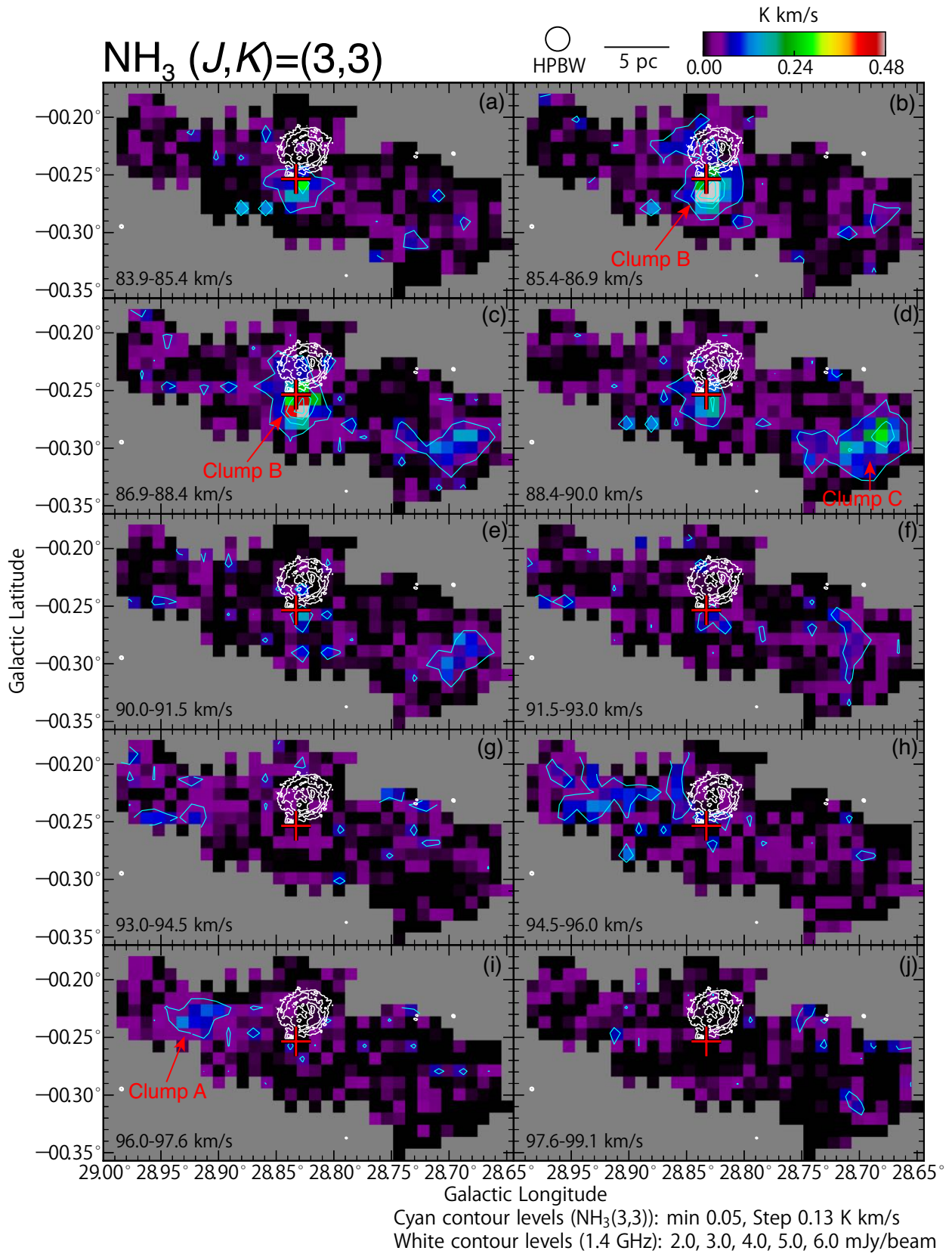


Fig. 6. Same as Figure 4, but for NH₃ (J, K) = (3, 3).

Figure 7(a) and (b) shows the peak velocity and line width map of the NH₃ (1,1) main line, respectively. Clump A, B, and C have different radial velocities at ~ 96 , ~ 87 , and ~ 89 km s⁻¹ (Figure 7a). We also find the 100 km s⁻¹ velocity component at $(l, b) \sim (28^\circ 72, -0^\circ 24)$ around the northwest side of Clump C. The line width of Clump A is ~ 2.3 km s⁻¹. Clump B has a large line width of ~ 3.0 km s⁻¹ around the methanol maser source shown in the cross mark. Finally, we point out that Clump C has a uniform line width of ~ 2.0 km s⁻¹.

3.3 Physical properties of NH₃ clumps

Following procedures, we estimated the physical parameters of three NH₃ clumps from our NH₃ data (Ho & Townes 1983; Ungerechts et al. 1986; Mangum et al. 1992; Mangum & Shirley 2015). First of all, we defined the clump radius (r) by

$$r = \sqrt{\frac{S}{\pi}}, \quad (1)$$

where S is the clump area detected above 3σ , assuming spherical shapes of the NH₃ (1,1) and NH₃ (2,2) emission. The radius of Clump A, B, and C is ~ 2 pc, ~ 3 pc, and ~ 3 pc, respectively.

Then, we estimated the optical depth (τ), rotational temperature (T_{rot}), and total column density (N_{TOT}). The optical depth [$\tau(1, 1, m)$] of the NH₃ (1,1) main line was derived from the intensity ratio of the main and satellite line above 2σ using the following equation.

$$\frac{T_{\text{MB}}(\text{main})}{T_{\text{MB}}(\text{sate})} = \frac{1 - e^{-\tau(1, 1, m)}}{1 - e^{-a\tau(1, 1, m)}}, \quad (2)$$

where T_{MB} is the main-beam temperature, a is the theoretical intensity ratio, the main to the inner and outer-satellite lines are $a = 0.278$ and $a = 0.222$, respectively (McGary & Ho 2002). In this paper, we adopted the median value of four optical depths derived from the ratios of the main to four satellite lines. The mean optical depth in Clump A, B, and C are 1.4 ± 0.6 , 1.6 ± 0.7 , and 1.7 ± 0.9 , respectively. The error shows the standard deviations of the mean value.

We estimated the rotational temperature from the NH₃ (2,2)/(1,1) intensity ratio of the main line detected above 3σ . If we assume that the same line widths of NH₃ (1,1) and NH₃ (2,2) (e.g., Urquhart et al. 2011; Wienen et al. 2018), the rotational temperature is given by

$$T_{\text{rot}}(2, 2 : 1, 1) = -41.1 \left/ \ln \left[\left(\frac{-0.282}{\tau(1, 1, m)} \right) \times \ln \left\{ 1 - \frac{T_{\text{MB}}(2, 2, m)}{T_{\text{MB}}(1, 1, m)} \times (1 - e^{-\tau(1, 1, m)}) \right\} \right] \right. [K]. \quad (3)$$

We converted the rotational temperature to kinetic temperature (T_{kin}) by adopting the Monte Carlo

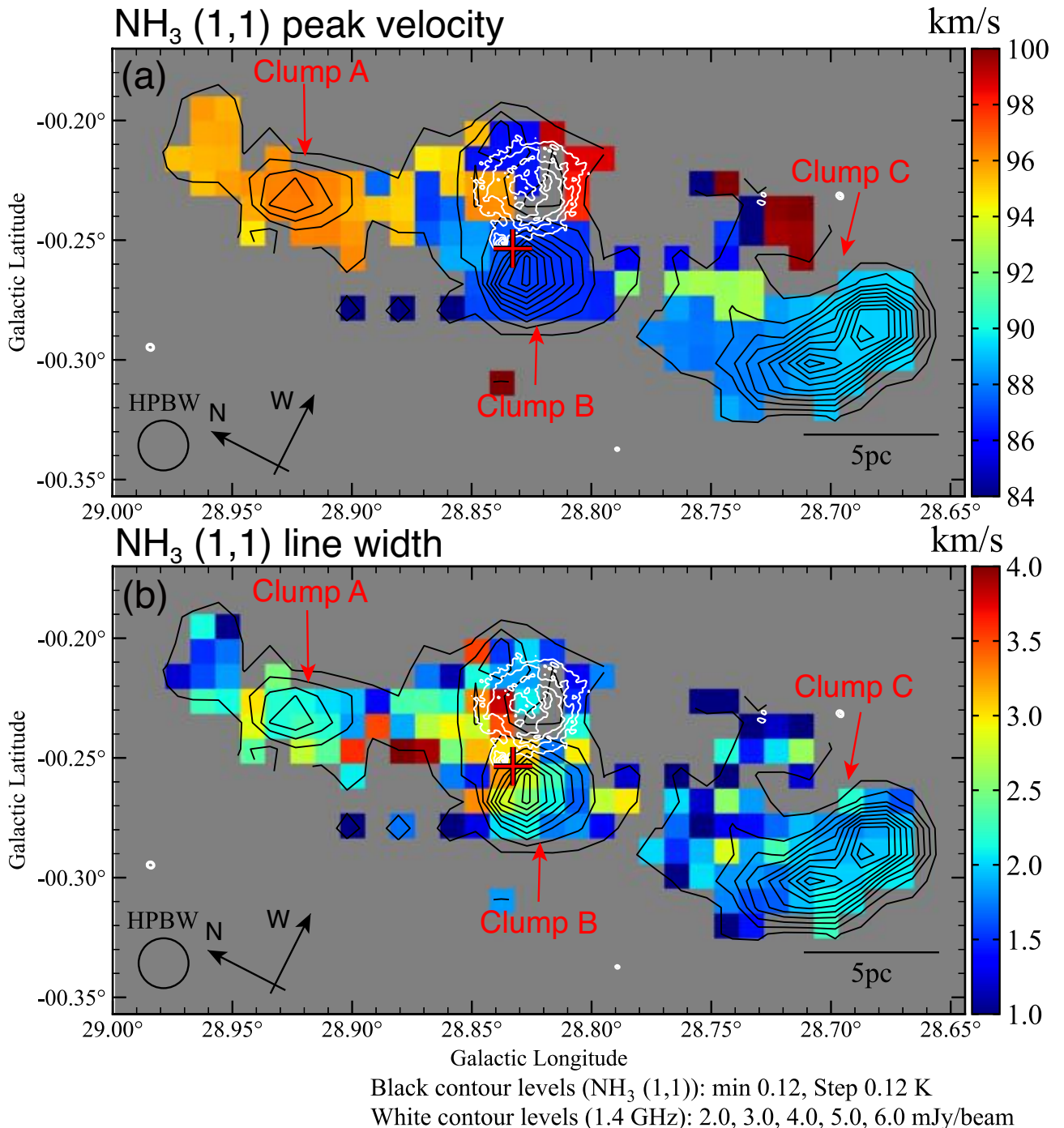


Fig. 7. (a) Peak velocity and (b) velocity width maps of the NH₃ (J, K) = (1, 1) line resulting from a Gaussian function fitted to the emission within pixels above 0.12 K ($> 4\sigma$). The black contours show the NH₃ (J, K) = (1, 1) peak intensity. The lowest black contour level and intervals are 0.12 K ($\sim 4\sigma$). The red cross and white contours are the same as in Figure 2a. The white contour levels of the VLA 1.4 GHz continuum image are 2.0, 3.0, 4.0, 5.0, and 6.0 mJy/beam.

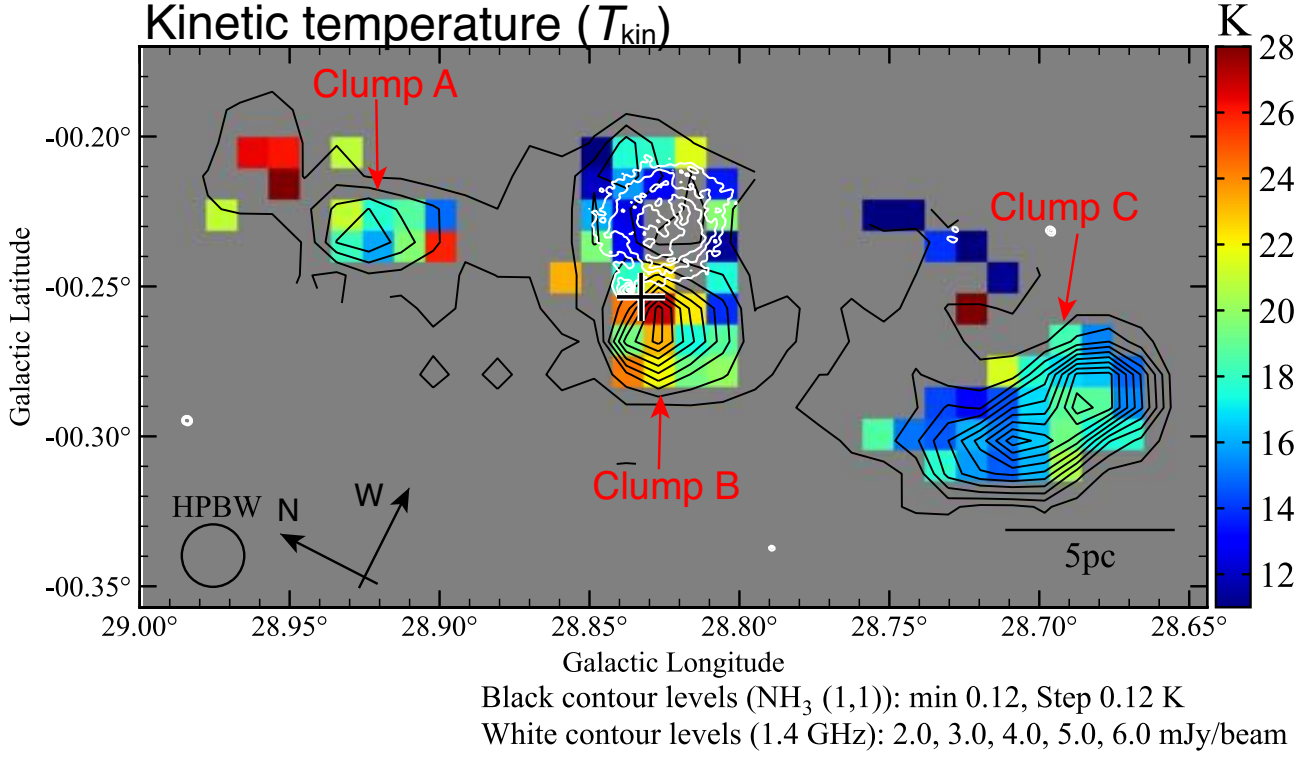


Fig. 8. The kinetic temperature map obtained by the (2,2)/(1,1) integrated intensity ratio above the 3σ noise level. The black contours show the $\text{NH}_3 (J, K) = (1, 1)$ peak intensity. The lowest black contour level and intervals are 0.12 K ($\sim 4\sigma$). The black cross and white contours are the same as in Figure 2a. The white contour levels of the VLA 1.4 GHz continuum image are 2.0, 3.0, 4.0, 5.0, and 6.0 mJy/beam.

method (Appendix B of Tafalla et al. 2004). The error of the kinetic temperature and rotational temperature was calculated by the error of the Gaussian fitting toward the peak intensity of $\text{NH}_3 (1, 1)$, $\text{NH}_3 (2, 2)$, and satellite lines.

$$T_{\text{kin}} = T_{\text{rot}} \left/ \left\{ 1 - \frac{T_{\text{rot}}}{41.1} \ln \left[1 + 1.1 \exp \left(-\frac{16}{T_{\text{rot}}} \right) \right] \right\} \right. [\text{K}] \quad (4)$$

Figure 8 presents the kinetic temperature distribution. The center of Clump A has $T_{\text{kin}} = 17.7 \pm 0.1$ K, and the northern part at $(l, b) \sim (28^\circ 96, -0^\circ 206)$ has a high temperature of $T_{\text{kin}} = 26.4 \pm 0.3$ K. Clump B around the methanol maser source is enhanced of $T_{\text{kin}} = 27.0 \pm 0.6$ K. This peak value is consistent with $T_{\text{dust}} \sim 27$ K obtained by the Herschel continuum image (see Figure 8a in Dewangan et al. 2017). Clump C has uniform temperature distribution of $T_{\text{kin}} \sim 14\text{-}18$ K.

We calculated the NH_3 column density from the $\text{NH}_3 (1,1)$ and $\text{NH}_3 (2,2)$ data points above 3σ . The $\text{NH}_3 (1,1)$ column density assuming Local Thermal Equilibrium (LTE) is given by

$$N(1,1) = 2.78 \times 10^{13} \tau(1,1, m) \left(\frac{T_{\text{rot}}}{[\text{K}]} \right) \left(\frac{\Delta v}{[\text{km s}^{-1}]} \right) [\text{cm}^{-2}], \quad (5)$$

Table 3. Physical parameters in each NH₃ clump

Name	Radius [pc]	$\tau(1,1,m)$ (3)	T_{rot} [K] (4)	T_{kin} [K] (5)	$N_{\text{tot}}(\text{NH}_3)$ [cm ⁻²] (6)	$N(\text{H}_2)$ [cm ⁻²] (7)	M_{LTE} [M_{\odot}] (8)
Clump A	1.6	1.4 ± 0.6	16.5 ± 2.0	19.2 ± 3.0	$(2.9 \pm 1.0) \times 10^{15}$	$(1.2 \pm 0.4) \times 10^{23}$	2.0×10^4
Clump B	2.8	1.6 ± 0.7	15.4 ± 3.9	17.9 ± 5.2	$(4.3 \pm 2.2) \times 10^{15}$	$(1.7 \pm 0.9) \times 10^{23}$	9.5×10^4
Clump C	2.8	1.5 ± 0.6	14.6 ± 1.5	16.5 ± 2.1	$(3.2 \pm 1.2) \times 10^{15}$	$(1.3 \pm 0.5) \times 10^{23}$	7.1×10^4

Columns: (1) Clump name (2) The clump radius defined above 3σ of the NH₃ (1,1) and NH₃ (2,2) emission. (3) The mean value of optical depth.

(4) The mean value of rotational temperature. (5) The mean value of the kinetic temperature. (6) The mean value of the total NH₃ column density.

(7) The mean value of H₂ column density. (8) The total LTE mass of a clump. The errors are derived by the standard deviation of the mean value in each clump.

where Δv is the line width of the main line. Furthermore, the NH₃ column density (Turner 1991; Wilson et al. 2013) summing up the total energy levels is given by

$$N_{\text{TOT}}(\text{NH}_3) = \frac{N(J,K)}{g_J \cdot g_I \cdot g_K} Q_{\text{rot}} \exp\left(\frac{E_u(J,K)}{kT_{\text{rot}}}\right) \quad (6)$$

$$\sim N(1,1) \left[\frac{1}{3} \exp\left(\frac{23.3}{T_{\text{rot}}}\right) + 1 + \frac{5}{3} \exp\left(\frac{-41.1}{T_{\text{rot}}}\right) + \frac{14}{3} \exp\left(\frac{-100.2}{T_{\text{rot}}}\right) \right], \quad (7)$$

where Q_{rot} is the partition function expressed as follows.

$$Q_{\text{rot}} = \sum_J \sum_K g_J \cdot g_I \cdot g_K \exp\left(-\frac{E_u(J,K)}{kT_{\text{rot}}}\right), \quad (8)$$

where g_J is rotational degeneracy, g_I is nuclear spin degeneracy, g_K is K-degeneracy, k is Boltzmann constant, and $E_u(J,K)$ is the upper energy level of inversion transition from the grand state, respectively. The uncertainties of total column densities were estimated by taking into account errors in the rotational temperature.

Figure 9 shows the NH₃ total column density map. Clump B has a high column density of $(9.1 \pm 0.4) \times 10^{15}$ cm⁻² at $(l,b) = (28^\circ 837, -0^\circ 247)$, which coincides with the UCH II region. In contrast, Clump A and C have a low of $(1.8_{-0.08}^{+0.09}) \times 10^{15}$ cm⁻² and $\sim (3.7 \pm 0.3) \times 10^{15}$ cm⁻², respectively. These values correspond to $\sim 3.6 \times 10^{23}$ cm⁻², $\sim 7.2 \times 10^{22}$ cm⁻², and $\sim 1.5 \times 10^{23}$ cm⁻² of the H₂ column density, respectively. We used the $N(\text{NH}_3)$ to $N(\text{H}_2)$ conversion factor of $X(\text{NH}_3) = 2.5 \times 10^{-8}$ derived from the massive star-forming regions in the Galactic plane (Urquhart et al. 2015). The peak H₂ column density around the methanol maser source is factor 4 larger than $\sim 9 \times 10^{22}$ cm⁻² obtained by the Herschel dust continuum image (Dewangan et al. 2017).

The LTE mass is estimated by

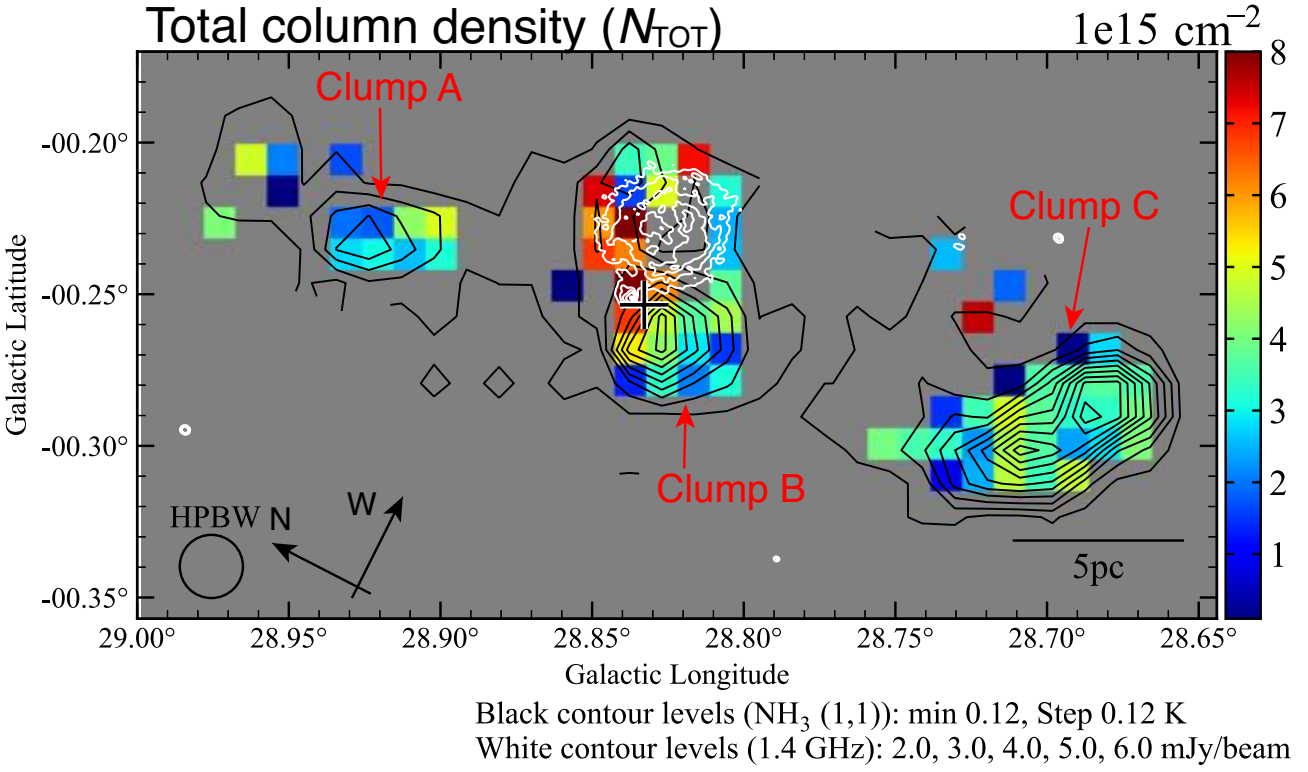


Fig. 9. The NH_3 total column density map above the 3σ noise level. The contours show the $\text{NH}_3 (J, K) = (1, 1)$ peak intensity. The lowest black contour level and intervals are 0.12 K ($\sim 4\sigma$). The black cross and white contours are the same as in Figure 2a. The white contour levels of the VLA 1.4 GHz continuum image are 2.0, 3.0, 4.0, 5.0, and 6.0 mJy/beam.

$$M_{\text{LTE}} = \mu_{\text{H}_2} m_{\text{H}} D^2 \sum_i \Omega N_i(\text{H}_2), \quad (9)$$

where $\mu_{\text{H}_2} \sim 2.8$ is the mean molecular weight per hydrogen molecule (Appendix A.1 in Kauffmann et al. 2008), $m_{\text{H}} = 1.67 \times 10^{-24} \text{ g}$ is the proton mass, $D = 5.07 \text{ kpc}$ is the distance to N49, $N_i(\text{H}_2)$ is the H_2 column density at the i th pixel, and Ω is the solid angle of each grid. The LTE mass of Clump A, Clump B, and Clump C is $2.0 \times 10^4 M_{\odot}$, $9.5 \times 10^4 M_{\odot}$, and $7.1 \times 10^4 M_{\odot}$, respectively. Dewangan et al. (2017) identified the dust clumps using the Herschel far-infrared continuum data (see Figure 9 and Table 1 in Dewangan et al. 2017). Our identified three NH_3 clumps of A, B, and C correspond to their dust clumps of #15 ($M_{\text{clump}} = 5.5 \times 10^3 M_{\odot}$), #12-#13 ($M_{\text{clump}} = 2.0 \times 10^4 M_{\odot}$), and #7-#8-#9 ($M_{\text{clump}} = 1.5 \times 10^4 M_{\odot}$), respectively. We point out that the mass of clump #12-#13 and clump #7-#8-#9 is the sum of the individual Herschel clumps in Dewangan et al. (2017). The LTE mass calculated from NH_3 data is factor 4-5 larger than the dust clump mass estimated by Dewangan et al. (2017). Table 3 presents the physical parameters of each NH_3 clump. The errors were estimated by the standard deviation of the mean value in each clump.

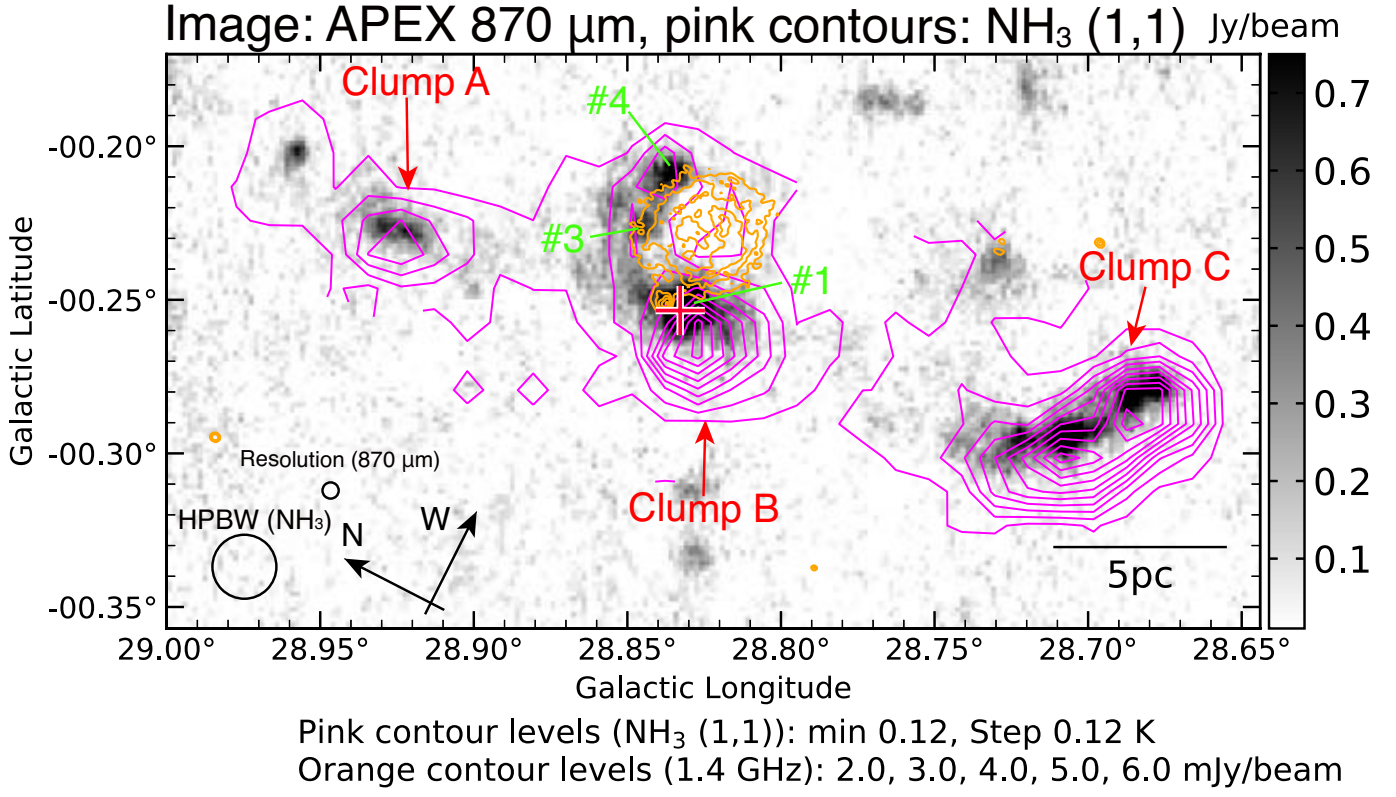


Fig. 10. The NH_3 ($J, K = (1, 1)$) peak intensity shown as pink contours superposed on the APEX 870 μm continuum image. The lowest pink contour level and intervals are 0.12 K ($\sim 4\sigma$). The red cross is the same as in Figure 2a. The orange contour levels of the VLA 1.4 GHz continuum image are 2.0, 3.0, 4.0, 5.0, and 6.0 mJy/beam. #1, #3, and #4 indicate the dust condensations identified by Deharveng et al. (2010).

4 Discussion

4.1 Distributions of cold dust condensations and star formation in NH_3 clumps

Figure 10 shows the NH_3 distributions presented by pink contours superposed on the 870 μm dust continuum image. We point out Clump A, B, and C corresponding to the dust condensations of AGAL028.922-00.227⁹, AGAL028.831-00.252¹⁰, and AGAL028.707-00.294¹¹, respectively. These dust clumps were identified by the ATLASGAL survey (Csengeri et al. 2014; Urquhart et al. 2014). The dust peak also exists at $(l, b) \sim (28^\circ.96, -0^\circ.20)$, which is the northern side of Clump A. The NH_3 peaks of Clump B coincide with three dust condensations of #1, #3, and #4 along with the edge of the N49 bubble (see also Figure 18 in Deharveng et al. 2010).

Figure 11 presents the distributions of YSOs identified by Dirienzo et al. (2012). The image and pink contours show the Spitzer 8 μm and peak intensity of NH_3 (1,1), respectively. Dirienzo et

⁹ https://atlasgal.mpifr-bonn.mpg.de/cgi-bin/ATLASGAL_SEARCH_RESULTS.cgi?text_field_1=AGAL028.922-00.227

¹⁰ https://atlasgal.mpifr-bonn.mpg.de/cgi-bin/ATLASGAL_SEARCH_RESULTS.cgi?text_field_1=AGAL028.831-00.252

¹¹ https://atlasgal.mpifr-bonn.mpg.de/cgi-bin/ATLASGAL_SEARCH_RESULTS.cgi?text_field_1=AGAL028.707-00.294

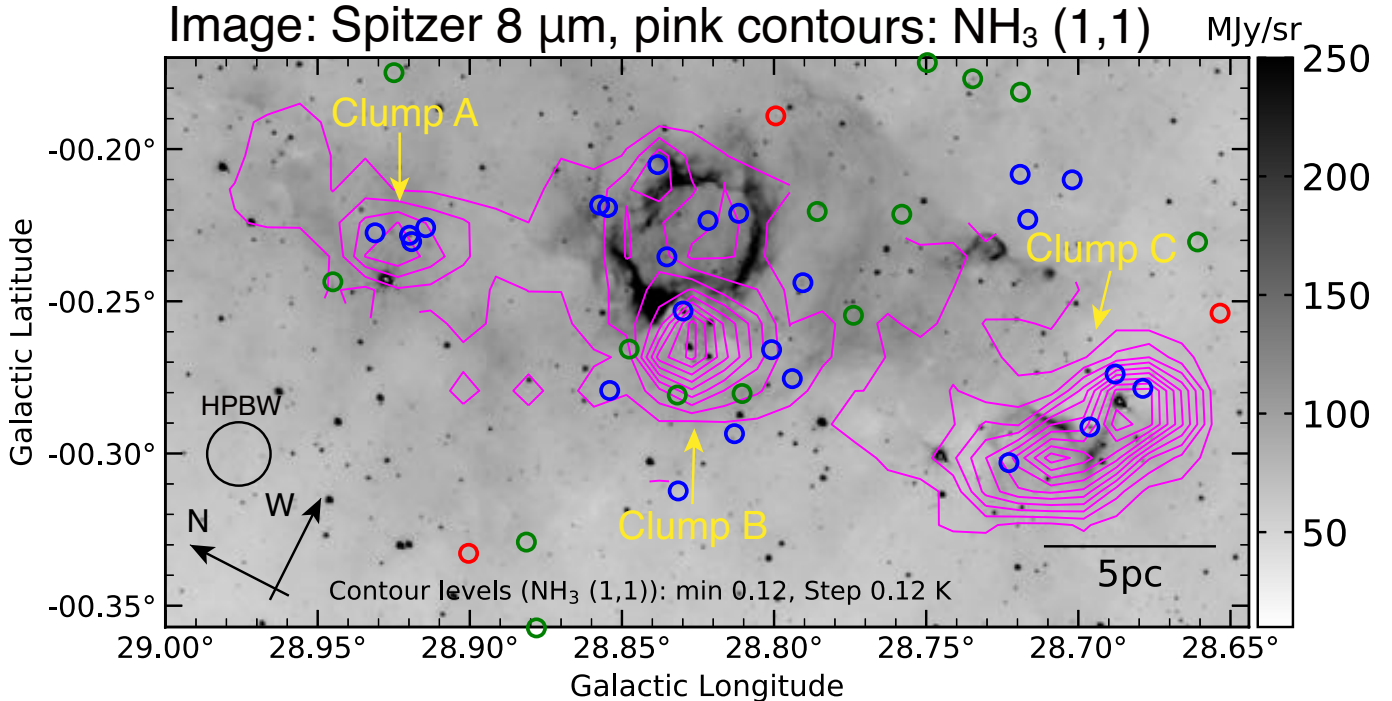


Fig. 11. YSO distributions superposed on the Spitzer 8 μm continuum image. Pink contours indicate the NH_3 (J, K) = (1, 1) peak intensity. The lowest pink contour level and intervals are 0.12 K ($\sim 4\sigma$). Blue, green, red circles show the Stage I, Stage II, and Stage III YSOs identified by Dirienzo et al. (2012) based on the classification model of Robitaille et al. (2006).

al. (2012) classified YSOs to “Stage I, Stage II, and Stage III” with their evolutional stage defined by Robitaille et al. (2006). Clump A and C have Stage I YSOs shown in blue circles. Clump B has Stage I YSOs at the edge and inside the bubble. Stage II YSOs exist on the eastern side of Clump B. We suggest that the low mass star formation proceeds at each NH_3 clump in the molecular filament because YSOs exist at each dense clump. Clump A and C exists at ~ 5 pc and ~ 10 pc away from the edge of the bubble traced by the 1.4 GHz radio continuum image. Therefore, we propose that these clumps might not be affected by the external shock compression or ionization from the N49 bubble, but the sites of spontaneous star formation. Clump C has low kinetic temperatures of 14–18 K (Figure 8) and the uniform line width of $\sim 2.0 \text{ km s}^{-1}$ (Figure 7b), while it includes NH_3 dense gas, cold dust condensation, and Stage I YSOs (Figure 10). We suppose that they show signatures of the early stage of star formation in Clump C. Clump A and C are not detected in the radio continuum emission even though dust condensations and YSOs. Therefore, these clumps might be the more initial stage or small scale of star formation than Clump B.

4.2 Impact of the N49 bubble to the NH_3 clump

The NH_3 (1,1) main line has a large line width of $3.8 \pm 0.3 \text{ km s}^{-1}$ at $(l, b) = (28^\circ 837, -0^\circ 226)$, which

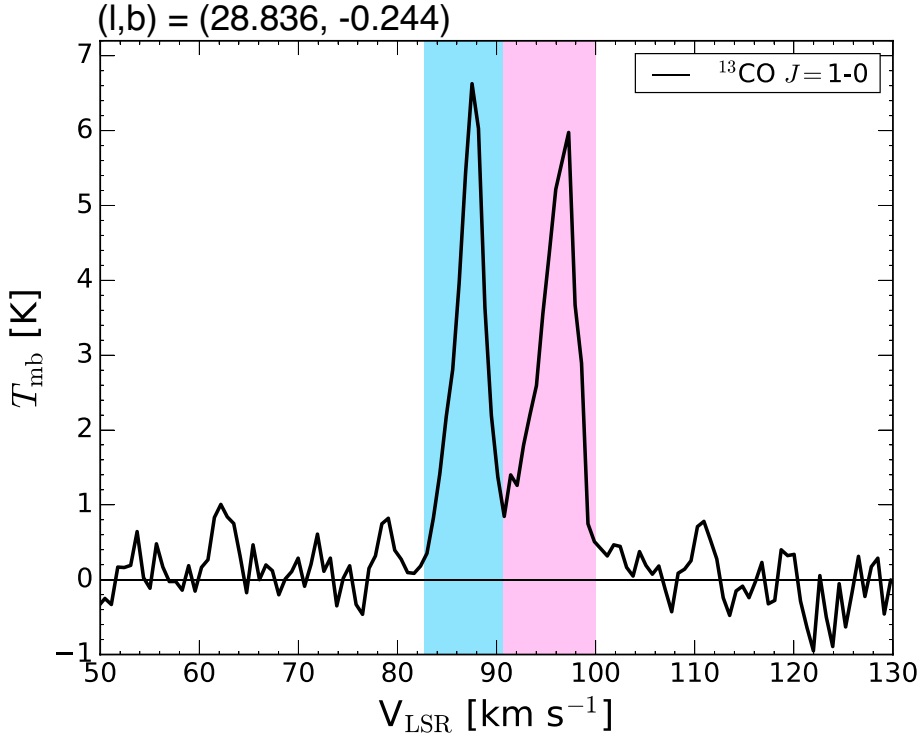


Fig. 12. The FUGIN ^{13}CO spectra at $(l, b) = (28.^\circ 836, -0.^\circ 244)$. Blue and pink area show the integrated velocity range of the two molecular filaments in Figure 13(a) and 13(b), respectively.

corresponds to the northern interface of Clump B and ionized gas (Figure 7b). This result suggests that the turbulent motion is enhanced locally by the interaction of gas within the bubble and the NH_3 dense clump. The distributions of kinetic temperature have a local high $T_{\text{kin}} = 27.0 \pm 0.6$ K at the 6.7 GHz methanol maser source associated with MYSOs (Cyganowski et al. 2009), while it has a low $T_{\text{kin}} < 18$ K at the northern and western edge of the bubble (Figure 8). We propose that this shows the feedback from the young ($< 10^5$ yr) embedded MYSOs are heating the dense clump locally. Our previous studies support this result (e.g., Monkey Head nebula: Chibueze et al. 2013, AFGL-333: Nakano et al. 2017, W33: Murase et al. 2022, and Sh 2-255: Kohno et al. 2022). These papers concluded that embedded cluster and the compact H II region with their age of $< 10^5$ yr can affect the local heating of the dense NH_3 clump.

4.3 Two molecular filaments and triggered star formation

Figure 12 shows the FUGIN ^{13}CO $J = 1-0$ spectra at the edge of the bubble. We can find the two velocity components of $\sim 88 \text{ km s}^{-1}$ and $\sim 95 \text{ km s}^{-1}$. Dewangan et al. (2017) reported the molecular filaments composed of these two velocity components from the ^{13}CO $J = 1-0$ Galactic Ring Survey data (Jackson et al. 2006). Figure 13(a) and (b) present NH_3 peak intensity distributions superposed

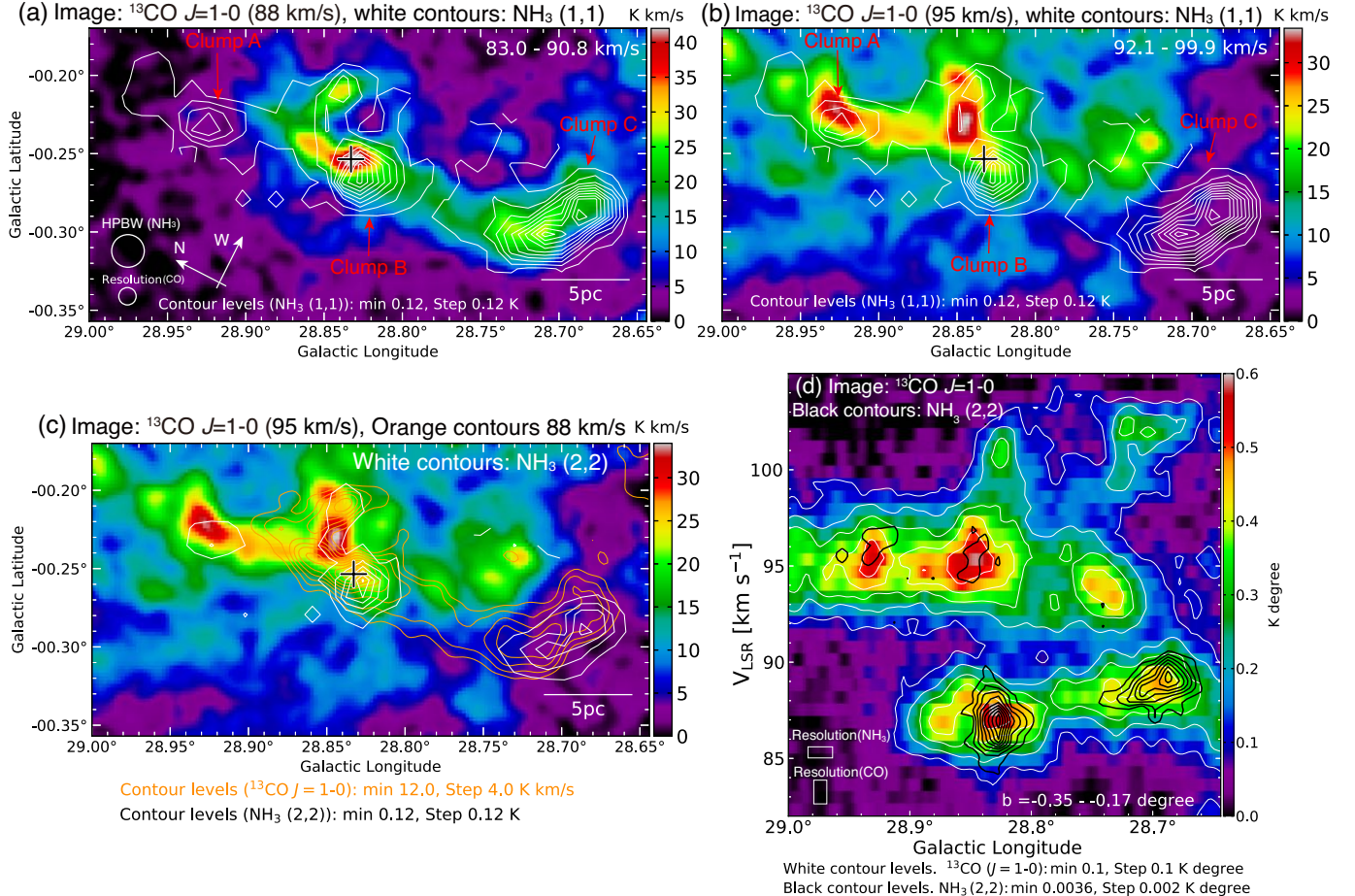


Fig. 13. The FUGIN ^{13}CO integrated intensity map of two molecular filaments identified by Dewangan et al. (2017). The integrated velocity range of (a) 83.0-90.8 km s⁻¹ and (b) 92.1-99.9 km s⁻¹, respectively. White contours indicate the NH_3 (J, K) = (1, 1) peak intensity. The lowest white contour level and intervals are 0.12 K ($\sim 4\sigma$). (c) The integrated intensities of the 88 km s⁻¹ component (orange contours) and 95 km s⁻¹ components (background image). White contours indicate the NH_3 (J, K) = (2, 2) peak intensity. The black cross is the same as in Figure 2a. (d) The longitude-velocity diagram of ^{13}CO J=1-0 shown as white contours. The lowest white contour level and intervals are 0.1 K degree. The black contours present the NH_3 (2,2) intensity of the same integrated latitude range. The lowest black contour level and intervals are 0.0036 K degree and 0.002 K degree, respectively.

on the molecular filaments of ~ 88 km s⁻¹ and ~ 95 km s⁻¹ components, respectively. The NH_3 peak of Clump B and C corresponds to the CO peak of the ~ 88 km s⁻¹ component. Clump A coincides with the CO peak of the ~ 95 km s⁻¹ component. Figure 13(c) demonstrates NH_3 (2,2) peak intensity overlaid on the two velocity components shown in the image of 95 km s⁻¹ and orange contours of 88 km s⁻¹. Clump B exists at the overlapped region of the two velocity components. This result supports the filament-filament collision-induced dense gas and massive star formation at the edge of the bubble proposed by Dewangan et al. (2017). Figure 13 (d) shows the longitude-velocity diagram. Black contours indicate the NH_3 (2,2) distribution. The 88 km s⁻¹ and 95 km s⁻¹ component connect with the bridge feature on the velocity space reported by Dewangan et al. (2017). This is evidence of

the collisional interaction of two clouds from the numerical simulation by Haworth et al. (2015) based on the model of Takahira et al. (2014). The NH_3 (2,2) peaks coincide with the ^{13}CO dense points of the 88 km s^{-1} and 95 km s^{-1} component. The NH_3 (2,2) intensity is more enhanced at 88 km s^{-1} than the 95 km s^{-1} component. We suggest that the dense gas produced by the shocked compression of filament collision is likely to exist at the 88 km s^{-1} component. Indeed, the numerical simulation showed that the shock compression by cloud-cloud collision induces dense gas formation traced by NH_3 (Priestley & Whitworth 2021). Therefore, our NH_3 results support that the current massive star and dense gas formation at the edge of the bubble was triggered by the collision event suggested by Dewangan et al. (2017).

5 Summary

The conclusions of our paper are summarized as follows:

1. We have performed the $\text{NH}_3 (J, K) = (1, 1), (2, 2)$, and $(3, 3)$ survey toward the Galactic infrared bubble N49 (G28.83-0.25) as a part of the KAGONMA project led by the Kagoshima University.
2. We found three NH_3 clumps (A, B, and C) along the molecular filament with the radial velocities of $\sim 96, 87$, and 89 km s^{-1} , respectively.
3. The kinetic temperature derived from the NH_3 (2,2)/ NH_3 (1,1) shows $T_{\text{kin}} = 27.0 \pm 0.6 \text{ K}$ enhanced at Clump B in the eastern edge of the bubble, where position coincides with MYSOs associated with the 6.7 GHz methanol maser source. This result shows the dense clump is locally heated by the stellar feedback from the embedded MYSOs.
4. The NH_3 Clump B also exists at the 88 km s^{-1} and 95 km s^{-1} molecular filament intersection. Therefore, we suggest that the filament-filament interaction scenario argued by Dewangan et al. (2017) can explain the NH_3 dense gas formation in Clump B.
5. The NH_3 Clump A and C at the northern and southern sides of the molecular filament exist $\sim 5 - 10 \text{ pc}$ apart from the edge of the bubble traced by the 1.4 GHz radio continuum image. This result suggests that these clumps are likely to occur in spontaneous star formation, not to be affected by the ionization feedback from the N49 bubble.

Acknowledgements

We are grateful to the anonymous referee for carefully reading our manuscript and giving us thoughtful suggestions, which greatly improved of the paper. The Nobeyama 45-m radio telescope is operated by Nobeyama Radio Observatory, a branch of the National Astronomical Observatory of Japan. The authors wish to thank all staff of the Nobeyama radio observatory for their assistance in our backup

observations. The NH₃ backup observations are promoted on a lot of contributions of Kagoshima university, so the authors would like to thank all them, Dr. Tatsuya Kamezaki, Dr. Gabor Orosz, Dr. Mitsuhiro Matsuo, Mr. Hideo Hamabata, Mr. Tatsuya Baba, Mr. Ikko Hoshihara, Mr. Kohei Mizukubo, Mr. Tatsuya Sera, and Mr. Masahiro Uesugi. I appreciated the curator members of the Astronomy section of Nagoya city science museum supporting my research works. The data of the FUGIN project was retrieved from the JVO portal (<http://jvo.nao.ac.jp/portal/>) operated by ADC/NAOJ. The data analysis was carried out at the Astronomy Data Center of the National Astronomical Observatory of Japan. The ATLASGAL project is a collaboration between the Max-Planck-Gesellschaft, the European Southern Observatory (ESO) and the Universidad de Chile. It includes projects E-181.C-0885, E-078.F-9040(A), M-079.C-9501(A), M-081.C-9501(A) plus Chilean data. This work is based in part on observations made with the Spitzer Space Telescope, which was operated by the Jet Propulsion Laboratory, California Institute of Technology under a contract with NASA.

References

- Astropy Collaboration, Robitaille, T. P., Tollerud, E. J., et al. 2013, A&A, 558, A33
 Astropy Collaboration, Price-Whelan, A. M., Sipőcz, B. M., et al. 2018, AJ, 156, 123
 Baug, T., Dewangan, L. K., Ojha, D. K., et al. 2016, ApJ, 833, 85. doi:10.3847/1538-4357/833/1/85
 Benjamin, R. A., Churchwell, E., Babler, B. L., et al. 2003, PASP, 115, 953. doi:10.1086/376696
 Burns, R. A., Handa, T., Omodaka, T., et al. 2019, PASJ, 71, 91. doi:10.1093/pasj/psz074
 Carey, S. J., Noriega-Crespo, A., Mizuno, D. R., et al. 2009, PASP, 121, 76. doi:10.1086/596581
 Castor, J., McCray, R., & Weaver, R. 1975, ApJL, 200, L107. doi:10.1086/181908
 Cheung, A. C., Rank, D. M., Townes, C. H., et al. 1968, Phys. Rev. Lett., 21, 1701.
 doi:10.1103/PhysRevLett.21.1701
 Cheung, A. C., Rank, D. M., Townes, C. H., et al. 1969, ApJL, 157, L13. doi:10.1086/180374
 Chibueze, J. O., Imura, K., Omodaka, T., et al. 2013, ApJ, 762, 17. doi:10.1088/0004-637X/762/1/17
 Churchwell, E., Povich, M. S., Allen, D., et al. 2006, ApJ, 649, 759. doi:10.1086/507015
 Churchwell, E., Watson, D. F., Povich, M. S., et al. 2007, ApJ, 670, 428. doi:10.1086/521646
 Churchwell, E., Babler, B. L., Meade, M. R., et al. 2009, PASP, 121, 213. doi:10.1086/597811
 Csengeri, T., Urquhart, J. S., Schuller, F., et al. 2014, A&A, 565, A75. doi:10.1051/0004-6361/201322434
 Cyganowski, C. J., Whitney, B. A., Holden, E., et al. 2008, AJ, 136, 2391. doi:10.1088/0004-6256/136/6/2391
 Cyganowski, C. J., Brogan, C. L., Hunter, T. R., et al. 2009, ApJ, 702, 1615. doi:10.1088/0004-637X/702/2/1615

- Deharveng, L., Zavagno, A., & Caplan, J. 2005, *A&A*, 433, 565. doi:10.1051/0004-6361:20041946
- Deharveng, L., Schuller, F., Anderson, L. D., et al. 2010, *A&A*, 523, A6. doi:10.1051/0004-6361/201014422
- Dewangan, L. K., Ojha, D. K., & Zinchenko, I. 2017, *ApJ*, 851, 140. doi:10.3847/1538-4357/aa9be2
- Dirienzo, W. J., Indebetouw, R., Brogan, C., et al. 2012, *AJ*, 144, 173. doi:10.1088/0004-6256/144/6/173
- Draine, B. T. & Li, A. 2007, *ApJ*, 657, 810. doi:10.1086/511055
- Draine, B. T. 2003, *ARA&A*, 41, 241. doi:10.1146/annurev.astro.41.011802.094840
- Dale, J. E., Bonnell, I. A., & Whitworth, A. P. 2007, *MNRAS*, 375, 1291. doi:10.1111/j.1365-2966.2006.11368.x
- Elmegreen, B. G. & Lada, C. J. 1977, *ApJ*, 214, 725. doi:10.1086/155302
- Elmegreen, B. G. 1998, *Origins*, 148, 150
- Enokiya, R. & Fukui, Y. 2022, *ApJ*, 931, 155. doi:10.3847/1538-4357/ac674f
- Everett, J. E. & Churchwell, E. 2010, *ApJ*, 713, 592. doi:10.1088/0004-637X/713/1/592
- Fukui, Y., Ohama, A., Kohno, M., et al. 2018, *PASJ*, 70, S46. doi:10.1093/pasj/psy005
- Fukui, Y., Habe, A., Inoue, T., et al. 2021, *PASJ*, 73, S1. doi:10.1093/pasj/psaa103
- Fujita, S., Torii, K., Tachihara, K., et al. 2019, *ApJ*, 872, 49. doi:10.3847/1538-4357/aafac5
- Fujita, S., Torii, K., Kuno, N., et al. 2021, *PASJ*, 73, S172. doi:10.1093/pasj/psz028
- Habe, A. & Ohta, K. 1992, *PASJ*, 44, 203
- Hanaoka, M., Kaneda, H., Suzuki, T., et al. 2019, *PASJ*, 71, 6. doi:10.1093/pasj/psy126
- Hanaoka, M., Kaneda, H., Suzuki, T., et al. 2020, *PASJ*, 72, 5. doi:10.1093/pasj/psz123
- Hasegawa, T., Sato, F., Whiteoak, J. B., et al. 1994, *ApJL*, 429, L77. doi:10.1086/187417
- Hattori, Y., Kaneda, H., Ishihara, D., et al. 2016, *PASJ*, 68, 37. doi:10.1093/pasj/psw028
- Haworth, T. J., Tasker, E. J., Fukui, Y., et al. 2015, *MNRAS*, 450, 10. doi:10.1093/mnras/stv639
- Helfand, D. J., Becker, R. H., White, R. L., et al. 2006, *AJ*, 131, 2525. doi:10.1086/503253
- Higuchi, A. E., Chibueze, J. O., Habe, A., et al. 2014, *AJ*, 147, 141. doi:10.1088/0004-6256/147/6/141
- Hirata, Y., Handa, T., Murase, T., et al. 2022, in preparation.
- Handa, T., Omodaka, T., Nagayama, T., et al. 2006, *Journal of Physics Conference Series*, 54, 42. doi:10.1088/1742-6596/54/1/007
- Ho, P. T. P. & Townes, C. H. 1983, *ARA&A*, 21, 239. doi:10.1146/annurev.aa.21.090183.001323
- Hosokawa, T. & Inutsuka, S.- ichiro . 2006, *ApJ*, 646, 240. doi:10.1086/504789
- Hunter, J. D. 2007, *Computing in Science and Engineering*, 9, 90
- Ikeda, M., Nishiyama, K., Ohishi, M., et al. 2001, *Astronomical Data Analysis Software and Systems X*, 238, 522
- Jackson, J. M., Rathborne, J. M., Shah, R. Y., et al. 2006, *ApJS*, 163, 145. doi:10.1086/500091
- Kamazaki, T., Okumura, S. K., Chikada, Y., et al. 2012, *PASJ*, 64, 29

- Kauffmann, J., Bertoldi, F., Bourke, T. L., et al. 2008, A&A, 487, 993. doi:10.1051/0004-6361:200809481
- Kawamura, A., Onishi, T., Yonekura, Y., et al. 1998, ApJS, 117, 387. doi:10.1086/313119
- Kohno, M., Torii, K., Tachihara, K., et al. 2018, PASJ, 70, S50. doi:10.1093/pasj/psx137
- Kohno, M., Tachihara, K., Torii, K., et al. 2021a, PASJ, 73, S129. doi:10.1093/pasj/psaa015
- Kohno, M., Tachihara, K., Fujita, S., et al. 2021b, PASJ, 73, S338. doi:10.1093/pasj/psy109
- Kohno, M., Omodaka, T., Handa, T., et al. 2022, PASJ, 74, 545. doi:10.1093/pasj/psac014
- Koide, N., Nakanishi, H., Sakai, N., et al. 2019, PASJ, 71, 113. doi:10.1093/pasj/psz101
- Kuno, N., et al. 2011, in Proc. 2011 XXXth URSI General Assembly and Scientific Symposium (New York: IEEE), 3670¹²
- Kutner, M. L., & Ulrich, B. L. 1981, ApJ, 250, 341
- Ladeyschikov, D. A., Bayandina, O. S., & Sobolev, A. M. 2019, AJ, 158, 233. doi:10.3847/1538-3881/ab4b4c
- Li, X., Esimbek, J., Zhou, J., et al. 2019, MNRAS, 487, 1517. doi:10.1093/mnras/stz1269
- Luisi, M., Anderson, L. D., Schneider, N., et al. 2021, Science Advances, 7, eabe9511. doi:10.1126/sciadv.abe9511
- Mangum, J. G., Wootten, A., & Mundy, L. G. 1992, ApJ, 388, 467. doi:10.1086/171167
- Mangum, J. G. & Shirley, Y. L. 2015, PASP, 127, 266. doi:10.1086/680323
- Mauch, T., Cotton, W. D., Condon, J. J., et al. 2020, ApJ, 888, 61. doi:10.3847/1538-4357/ab5d2d
- McGary, R. S. & Ho, P. T. P. 2002, ApJ, 577, 757. doi:10.1086/342233
- McGlynn, T., Scollick, K., & White, N. 1998, New Horizons from Multi-Wavelength Sky Surveys, 179, 465
- Minamidani, T., Nishimura, A., Miyamoto, Y., et al. 2016, Proc. SPIE, 9914, 99141Z. doi:10.1117/12.2232137
- Morris, M., Zuckerman, B., Palmer, P., et al. 1973, ApJ, 186, 501. doi:10.1086/152515
- Murase, T., Handa, T., Maebata, M., et al. 2020, Origins: From the Protosun to the First Steps of Life, 345, 353. doi:10.1017/S174392131900200X
- Murase, T., Handa, T., Hirata, Y., et al. 2022, MNRAS, 510, 1106. doi:10.1093/mnras/stab3472
- Nagahama, T., Mizuno, A., Ogawa, H., et al. 1998, AJ, 116, 336. doi:10.1086/300392
- Nagayama, T., Omodaka, T., Handa, T., et al. 2007, PASJ, 59, 869. doi:10.1093/pasj/59.5.869
- Nagayama, T., Omodaka, T., Handa, T., et al. 2009, PASJ, 61, 1023. doi:10.1093/pasj/61.5.1023
- Nakajima, T., Inoue, H., Fujii, Y., et al. 2019, PASJ, 71, S17
- Nakano, M., Soejima, T., Chibueze, J. O., et al. 2017, PASJ, 69, 16. doi:10.1093/pasj/psw120
- Nakanishi, H., Fujita, S., Tachihara, K., et al. 2020, PASJ, 72, 43. doi:10.1093/pasj/psaa027
- Nishimura, A., Minamidani, T., Umemoto, T., et al. 2018, PASJ, 70, S42
- Nishimura, A., Fujita, S., Kohno, M., et al. 2021, PASJ, 73, S285. doi:10.1093/pasj/psaa083

¹²<http://ieeexplore.ieee.org/xpl/articleDetails.jsp?arnumber=6051296>

- Ohama, A., Kohno, M., Fujita, S., et al. 2018, PASJ, 70, S47. doi:10.1093/pasj/psy012
- Perez, F., & Granger, B. E. 2007, Computing in Science and Engineering, 9, 21
- Pickett, H. M., Poynter, R. L., Cohen, E. A., et al. 1998, J. Quant. Spectrosc. Radiat. Transfer, 60, 883. doi:10.1016/S0022-4073(98)00091-0
- Purcell, C. R., Longmore, S. N., Walsh, A. J., et al. 2012, MNRAS, 426, 1972. doi:10.1111/j.1365-2966.2012.21800.x
- Palmeirim, P., Zavagno, A., Elia, D., et al. 2017, A&A, 605, A35. doi:10.1051/0004-6361/201629963
- Priestley, F. D. & Whitworth, A. P. 2021, MNRAS, 506, 775. doi:10.1093/mnras/stab1777
- Robitaille, T. P., Whitney, B. A., Indebetouw, R., et al. 2006, ApJS, 167, 256. doi:10.1086/508424
- Robitaille, T., & Bressert, E. 2012, APLpy: Astronomical Plotting Library in Python, ascl:1208.017
- Sato, K., Hasegawa, T., Umemoto, T., et al. 2021, PASJ, 73, 568. doi:10.1093/pasj/psab021
- Sault, R. J., Teuben, P. J., & Wright, M. C. H. 1995, Astronomical Data Analysis Software and Systems IV, 77, 433
- Sawada, T., Ikeda, N., Sunada, K., et al. 2008, PASJ, 60, 445
- Schuller, F., Menten, K. M., Contreras, Y., et al. 2009, A&A, 504, 415. doi:10.1051/0004-6361/200811568
- Sofue, Y., Kohno, M., Torii, K., et al. 2019, PASJ, 71, S1. doi:10.1093/pasj/psy094
- Solomon, P. M., Scoville, N. Z., & Sanders, D. B. 1979, ApJL, 232, L89. doi:10.1086/183042
- Tafalla, M., Myers, P. C., Caselli, P., et al. 2004, A&A, 416, 191. doi:10.1051/0004-6361:20031704
- Takahira, K., Tasker, E. J., & Habe, A. 2014, ApJ, 792, 63. doi:10.1088/0004-637X/792/1/63
- Takeba, N., Handa, T., Murase, T., et al. 2023, IAU Proceeding, in press.
- Thompson, M. A., Urquhart, J. S., Moore, T. J. T., et al. 2012, MNRAS, 421, 408. doi:10.1111/j.1365-2966.2011.20315.x
- Torii, K., Hasegawa, K., Hattori, Y., et al. 2015, ApJ, 806, 7. doi:10.1088/0004-637X/806/1/7
- Torii, K., Fujita, S., Nishimura, A., et al. 2019, PASJ, 71, S2. doi:10.1093/pasj/psz033
- Toujima, H., Nagayama, T., Omodaka, T., et al. 2011, PASJ, 63, 1259. doi:10.1093/pasj/63.6.1259
- Turner, B. E. 1991, ApJS, 76, 617. doi:10.1086/191577
- Ulich, B. L., & Haas, R. W. 1976, ApJS, 30, 247
- Umemoto, T., Minamidani, T., Kuno, N., et al. 2017, PASJ, 69, 78. doi:10.1093/pasj/psx061
- Ungerechts, H., Walmsley, C. M., & Winnewisser, G. 1986, A&A, 157, 207
- Urquhart, J. S., Morgan, L. K., Figura, C. C., et al. 2011, MNRAS, 418, 1689. doi:10.1111/j.1365-2966.2011.19594.x
- Urquhart, J. S., Csengeri, T., Wyrowski, F., et al. 2014, A&A, 568, A41. doi:10.1051/0004-6361/201424126
- Urquhart, J. S., Figura, C. C., Moore, T. J. T., et al. 2015, MNRAS, 452, 4029. doi:10.1093/mnras/stv1514
- van der Walt, S., Colbert, S. C., & Varoquaux, G. 2011, Computing in Science and Engineering, 13, 22

- Walmsley, C. M. & Ungerechts, H. 1983, A&A, 122, 164
- Watson, C., Povich, M. S., Churchwell, E. B., et al. 2008, ApJ, 681, 1341. doi:10.1086/588005
- Weaver, R., McCray, R., Castor, J., et al. 1977, ApJ, 218, 377. doi:10.1086/155692
- Werner, M. W., Roellig, T. L., Low, F. J., et al. 2004, ApJS, 154, 1. doi:10.1086/422992
- White, R. L., Becker, R. H., & Helfand, D. J. 2005, AJ, 130, 586. doi:10.1086/431249
- Whitworth, A. P., Bhattacharyya, A. S., Chapman, S. J., et al. 1994, MNRAS, 268, 291. doi:10.1093/mnras/268.1.291
- Wienen, M., Wyrowski, F., Schuller, F., et al. 2012, A&A, 544, A146. doi:10.1051/0004-6361/201118107
- Wienen, M., Wyrowski, F., Menten, K. M., et al. 2018, A&A, 609, A125. doi:10.1051/0004-6361/201526384
- Wilson, T. L., Rohlfs, K., & Hüttemeister, S. 2013, Tools of Radio Astronomy; Astronomy and Astrophysics Library. ISBN 978-3-642-39949-7. Springer-Verlag Berlin Heidelberg
- Xu, J.-L., Stutzki, J., Wu, Y., et al. 2019, Research in Astronomy and Astrophysics, 19, 183. doi:10.1088/1674-4527/19/12/183
- Xu, J.-L. & Ju, B.-G. 2014, A&A, 569, A36. doi:10.1051/0004-6361/201423952
- Yamada, R. I., Enokiya, R., Sano, H., et al. 2021, PASJ, 73, 880. doi:10.1093/pasj/psab050
- Yan, Q.-zeng, Xu, Y., Zhang, B., et al. 2016, AJ, 152, 117. doi:10.3847/0004-6256/152/5/117
- Zavagno, A., Deharveng, L., Comerón, F., et al. 2006, A&A, 446, 171. doi:10.1051/0004-6361:20053952
- Zavagno, A., Pomarès, M., Deharveng, L., et al. 2007, A&A, 472, 835. doi:10.1051/0004-6361:20077474
- Zavagno, A., Anderson, L. D., Russeil, D., et al. 2010, A&A, 518, L101. doi:10.1051/0004-6361/201014587